J. Fluid Mech. (2010), *vol.* 653, *pp.* 301–336.
doi:10.1017/S0022112010000248

Three-dimensional simulation of a flapping flag in a uniform flow

WEI-XI HUANG AND HYUNG JIN SUNG†

Department of Mechanical Engineering, KAIST 373-1, Guseong-dong, Yuseong-gu, Daejeon 305-701, Korea

(Received 15 May 2009; revised 11 January 2010; accepted 13 January 2010)

A three-dimensional computational model is developed for simulating the flag motion in a uniform flow. The nonlinear dynamics of the coupled fluid–flag system after setting up of flapping is investigated by a series of numerical tests. At low Reynolds numbers, the flag flaps symmetrically about its centreline when gravity is excluded, and the bending in the spanwise direction is observed near the corners on the trailing edge. As the Reynolds number increases, the spanwise bending is flattened due to the decrease of the positive pressure near the side edges as well as the viscous force of the fluid. At a certain critical Reynolds number, the flag loses its symmetry about the centreline, which is shown to be related to the coupled fluid–flag instability. The three-dimensional vortical structures shed from the flag show a significant difference from the results of two-dimensional simulations. Hairpin or O-shaped vortical structures are formed behind the flag by connecting those generated at the flag side edges and the trailing edge. Such vortical structures have a stabilization effect on the flag by reducing the pressure difference across the flag. Moreover, the positive pressure near the side edges is significantly reduced as compared with that in the center region, causing the spanwise bending. The Strouhal number defined based on the flag length is slightly dependent on the Reynolds number and the flag width, but scales with the density ratio as $St \sim \rho^{-1/2}$. On the other hand, the flapping-amplitude-based Strouhal number remains close to 0.2, consistent with the values reported for flying or swimming animals. A flag flapping under gravity is then simulated, which is directed along the negative spanwise direction. The sagging down of the flag and the rolling motion of the upper corner are observed. The dual effects of gravity are demonstrated, i.e. the destabilization effect like the flag inertia and the stabilization effect by increasing the longitudinal tension force.

1. Introduction

The flapping of flags in the wind is a commonplace and familiar phenomenon, yet still puzzles researchers due to its extremely complicated dynamics. Flapping dynamics is also an essential aspect of the tail and wing motions of swimming and flying animals. When a flag undergoes passive flapping, it exerts inertial and elastic forces on the fluid, while the fluid acts on the flag through pressure and viscosity. Together, these fluid–flag interactions can give rise to self-sustained oscillations at certain natural frequencies. Even for active flapping motions such as those of swimming and flying animals, the flapping frequency cannot be selected arbitrarily (Triantafyllou,

† Email address for correspondence: hjsung@kaist.ac.kr

Triantafyllou & Yue 2000; Fish & Lauder 2006). Recent studies have disclosed a simple relationship between the flapping frequency, amplitude and forward speed for a wide range of species of animals to fly or swim with high propulsive efficiency (Taylor, Nudds & Thomas 2003). When swimming in the wake of upstream obstacles or other animals, fishes were found to extract energy from surrounding fluid by synchronizing the flapping motion with environmental vortices and reaching a state of passive swimming (Liao *et al.* 2003; Beal *et al.* 2006; Eldredge & Pisani 2008; Jia & Yin 2008; Ristroph & Zhang 2008). Hence, the study of flapping behaviour sheds light on such biological processes. Moreover, flapping dynamics is also of importance in areas such as paper engineering (Watanabe *et al.* 2002*a*,*b*), socio-medical conditions like human snoring (Huang 1995; Balint & Lucey 2005), ocean/river power generation (Allen & Smits 2001; Taylor *et al.* 2001) and so on.

Fluid–structure interactions such as the flag-in-the-wind problem are a challenge to study by experiment and modelling on account of their complex geometries and freely moving boundaries. Researchers have risen to this challenge in an array of interesting studies (Païdoussis 2004). Taneda (1968) carried out experiments on a hanging flag in a wind tunnel and observed both the two- and three-dimensional oscillation modes of the waving motions. In the case of three-dimensional mode, one of the two corners on the trailing edge was found to roll up randomly. Zhang *et al.* (2000) visualized the motion of flexible filaments in a flowing soap film as a two-dimensional flag model. They found two distinct stable states for a single filament: the stretched-straight state and the self-sustained flapping state. More recently, Shelley, Vandenberghe & Zhang (2005) confirmed this bistable property in a water tunnel experiment using a heavy flexible sheet, and found that the non-dimensional flapping frequency is consistent with that of animal locomotion. For a two-dimensional flag, numerical simulations discovered three regimes, i.e. straight and stationary stable regime, regular flapping regime and chaotic flapping regime, by changing the flag-to-fluid mass ratio (Connell & Yue 2007) or the bending rigidity (Alben & Shelley 2008) or the free-stream velocity (Michelin, Llewellyn Smith & Glover 2008).

To predict the critical velocity of incoming flow for the onset of flapping of a flag (or flutter of a plate) and to compare with experimental data, various theoretical models were proposed for this fluid–flag coupled system. In these theoretical works, the flapping modes were assumed to be two-dimensional and linear beam models were usually adopted for the flag, while the fluid loads were obtained using certain approximations, e.g. Theodorsen's theory (Huang 1995, Argentina & Mahadevan 2005, Manela & Howe 2009*a*), potential flow theory (Guo & Païdoussis 2000) and slender-body theory (Lemaitre, Hémon & de Langre 2005). Furthermore, nonlinear flag models were developed based on the inextensibility condition to study the limit cycle oscillation state and the nature of bifurcation leading to flapping (Yadykin, Tenetov & Levin 2001; Tang, Yamamoto & Dowell 2003; Tang & Païdoussis 2007). The nonlinearity of the aerodynamics was also taken into account by solving the Navier–Stokes equations on a body-fitted mesh (Watanabe *et al.* 2002*a*; Balint & Lucey 2005). Moreover, the flag aspect ratio effect was investigated using a two-dimensional flag model by resorting to the data from a three-dimensional simulation (Argentina & Mahadevan 2005). A theoretical model for a plate with finite span immersed in a three-dimensional potential flow was reported in Eloy, Souilliez & Schouveiler (2007) and Eloy *et al.* (2008) by assuming a two-dimensional flutter motion. It was shown that a flag of finite spanwise width is more stable than that of infinite spanwise width. The development of new numerical methods and the improvement in computational power have made it an easy task to perform direct

simulations of a two-dimensional fluid flow interacting with flexible filaments or plates (Zhu & Peskin 2002; Farnell, David & Barton 2004; Huang, Shin & Sung 2007). However, few numerical studies have attempted to model a three-dimensional flag immersed in a viscous fluid flow. Kim & Peskin (2007) presented a three-dimensional flag flapping in wind as a numerical example of their penalty immersed boundary method by extending their two-dimensional filament formulation. Moreover, in the field of computer graphics, physically based models were introduced for simulating motion of cloth (Terzopoulos & Fleischer 1988; Li, Damodaran & Gay 1996).

In the present study, we sought to simulate a three-dimensional flapping flag in a uniform flow, manipulating in the framework of the immersed boundary method developed by Huang & Sung (2009). The flag motion equation is derived using the variational derivative of the deformation energy and solved on a Lagrangian grid. On the other hand, the Navier–Stokes equations are discretized on an Eulerian grid and solved by the fractional step method. The Eulerian fluid motion and the Lagrangian IB motion are connected by utilizing a smoothed approximation of the Dirac delta function (Peskin 2002). After developing the numerical method, we perform a series of simulations of the three-dimensional fluid–flag coupled system. The instantaneous flag motion is analysed under various conditions, and the surrounding vortical structures are identified. The flapping frequency is calculated and the effects of the flag width and density are evaluated. In this paper, we mainly focus on the nonlinear dynamics of the fluid–flag system after setting up of flapping by direct simulations, rather than finding the critical fluid velocity for the onset of flapping as in most of the previous studies. Although the flapping mode was usually assumed to be two-dimensional at the instability threshold (Eloy *et al.* 2007; Tang & Païdoussis 2007), the deflection along the spanwise direction occurs for large-amplitude flapping due to the fluid loading. Moreover, the cases with gravity included in the simulation are also studied where the sagging down of the flag occurs. These three-dimensional effects on the flag flapping dynamics are investigated numerically in detail, because these phenomena are so familiar to us but only few previous studies have taken into account these effects so far (Shelley *et al.* 2005; Kim & Peskin 2007). In § 2, we propose the formulation for the fluid–flag system and briefly describe the numerical method. The results and discussion are presented in § 3. We first consider the gravity-free case in §§ 3.1–3.3, where several issues are addressed including the spanwise bending of the flag, visualization of the surrounding flow field and effects of the Reynolds number, the flag density and the flag width. Then, in § 3.4 the effect of gravity on the flapping flag is discussed. Finally, a summary of the present study is given in § 4.

2. Problem formulation and numerical method

2.1. *Flag motion*

The flag motion is described by Lagrangian variables. A curvilinear coordinate system (s_1, s_2) is attached to the flag, as shown in figure 1. Among the four boundaries, one is fixed at $s_1 = 0$, which is aligned along the z-axis, while the other three are free boundaries. The longitudinal coordinate s_1 ranges from 0 to L, and the spanwise coordinate s_2 ranges from 0 to H, where L and H denote the length and width of the flag, respectively. Kim & Peskin (2007) used a cylindrical flagpole at the leading edge of the flag, which is aligned with the top edge but is extended below the bottom edge. Here we neglect the flagpole to keep the symmetry of geometry about the flag centreline, i.e. $s_2 = H/2$, and to exclude the influence of vortex shedding from the flagpole (Manela & Howe 2009*b*).

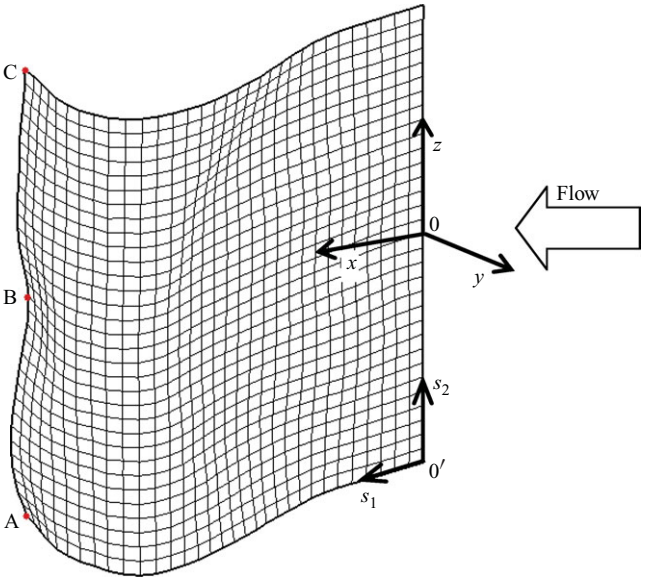

FIGURE 1. Schematic of the Lagrangian grid system and its curvilinear coordinates (s_1, s_2) on the flag. Points A, B and C denote the lower corner, the midpoint and the upper corner on the trailing edge, respectively.

To derive the formulation of the elastic force along the flag, we start from the principle of virtual work and use the variational derivative of the elastic energy. Let $\boldsymbol{X}(s_1, s_2, t)$ denote the Cartesian coordinates of an arbitrary point on the flag at time t. Depending on the material properties, the elastic energy stored in the flag can be expressed as a certain function of deformations, including stretching, shearing, bending and twisting. Here we use the following form

$$E(\boldsymbol{X}) = \int_S \sum_{i,j=1}^{2} \left[c_{ij}^T \left(T_{ij} - T_{ij}^0 \right)^2 + c_{ij}^B \left(B_{ij} - B_{ij}^0 \right)^2 \right] \mathrm{d}s_1 \, \mathrm{d}s_2 \tag{1}$$

where $T_{ij} = (\partial \boldsymbol{X}/\partial s_i \cdot \partial \boldsymbol{X}/\partial s_j)$ denotes the stretching and shearing effects, $B_{ij} = ((\partial^2 \boldsymbol{X}/\partial s_i \partial s_j) \cdot (\partial^2 \boldsymbol{X}/\partial s_i \partial s_j))^{1/2}$ denotes the bending and twisting effects, c_{ij}^T and c_{ij}^B are the corresponding coefficients and summation convention is not applied on both i and j. In (1), the superscript '0' denotes the initial value; we use

$$\boldsymbol{T}^0 = \begin{pmatrix} 1 & 0 \\ 0 & 1 \end{pmatrix} \quad \text{and} \quad \boldsymbol{B}^0 = \begin{pmatrix} 0 & 0 \\ 0 & 0 \end{pmatrix},$$

thereby setting the flag in an initially flat state. In this study, we assume that the flag material is inextensible in both the s_1 and s_2 directions; for simplicity, this constraint is imposed by making the stretching coefficients c_{11}^T and c_{22}^T sufficiently large. Moreover, large c_{12}^T and c_{21}^T are also used to resist in-plane shear. Note that the elastic energy defined in (1) is invariant to rigid motions of the flag.

The elastic force $\boldsymbol{F}_e$ is then obtained by using the variational derivative of the energy functional $E(\boldsymbol{X})$ (cf. Appendix A) and is expressed as

$$\boldsymbol{F}_e = \sum_{i,j=1}^{2} \left[\frac{\partial}{\partial s_i} \left(\sigma_{ij} \frac{\partial \boldsymbol{X}}{\partial s_j} \right) - \frac{\partial^2}{\partial s_i \partial s_j} \left(\gamma_{ij} \frac{\partial^2 \boldsymbol{X}}{\partial s_i \partial s_j} \right) \right], \tag{2}$$

where $\sigma_{ij} = 4c_{ij}^T(T_{ij} - T_{ij}^0)$ and $\gamma_{ij} = 2c_{ij}^B$ $(i, j = 1, 2)$. In the following, we use $\varphi_{ij} = 4c_{ij}^T$ as the stretching and shearing coefficients and γ_{ij} as the bending and twisting coefficients. Note that a different formulation of B_{ij} is used in (1) from that of Huang & Sung (2009), which results in a different expression of γ_{ij} and physically denotes different material properties.

After obtaining the elastic force, we can write the governing equation of the flag motion in the following form:

$$\rho_1 \frac{\partial^2 \boldsymbol{X}}{\partial t^2} = \sum_{i,j=1}^{2} \left[\frac{\partial}{\partial s_i} \left(\sigma_{ij} \frac{\partial \boldsymbol{X}}{\partial s_j} \right) - \frac{\partial^2}{\partial s_i \partial s_j} \left(\gamma_{ij} \frac{\partial^2 \boldsymbol{X}}{\partial s_i \partial s_j} \right) \right] + \rho_1 \boldsymbol{g} - \boldsymbol{F}, \tag{3}$$

where ρ_1 denotes the extra flag area density, $\boldsymbol{g}$ denotes gravity and $\boldsymbol{F}$ denotes the Lagrangian forcing exerted on the flag by the surrounding fluid. Note that the surrounding fluid density has been subtracted from ρ_1, and the actual flag area density should be $\rho_1 + c\rho_0$, where ρ_0 is the fluid density and c is the flag thickness. We introduce the following characteristic scales; the flag length L for the length, L/U_∞ for the time, where U_∞ denotes the far-field velocity, $\rho_1 U_\infty^2 / L$ for the Lagrangian forcing $\boldsymbol{F}$, $\rho_1 U_\infty^2$ for the stretching and shearing coefficients φ_{ij} as well as σ_{ij} and $\rho_1 U_\infty^2 L^2$ for the bending and twisting coefficients γ_{ij}. Thus, (3) can be written in the non-dimensional form

$$\frac{\partial^2 \boldsymbol{X}}{\partial t^2} = \sum_{i,j=1}^{2} \left[\frac{\partial}{\partial s_i} \left(\sigma_{ij} \frac{\partial \boldsymbol{X}}{\partial s_j} \right) - \frac{\partial^2}{\partial s_i \partial s_j} \left(\gamma_{ij} \frac{\partial^2 \boldsymbol{X}}{\partial s_i \partial s_j} \right) \right] + Fr \frac{\boldsymbol{g}}{g} - \boldsymbol{F}, \tag{4}$$

where $Fr = gL/U_\infty^2$ denotes the Froude number with $g = |\boldsymbol{g}|$. For convenience, the dimensionless quantities in (4) are written in the same form as their dimensional counterparts. At the fixed boundary, we consider the simply supported condition in the simulation, i.e.

$$\boldsymbol{X} = (0, 0, s_2), \quad \frac{\partial^2 \boldsymbol{X}}{\partial s_1^2} = 0 \quad \text{at } s_1 = 0. \tag{5}$$

At the free boundaries, we have

$$\frac{\partial^2 \boldsymbol{X}}{\partial s_1^2} = 0, \quad \frac{\partial^3 \boldsymbol{X}}{\partial s_1^3} = 0 \quad \text{at} \quad s_1 = L, \tag{6}$$

$$\frac{\partial^2 \boldsymbol{X}}{\partial s_2^2} = 0, \quad \frac{\partial^3 \boldsymbol{X}}{\partial s_2^3} = 0 \quad \text{at} \quad s_2 = 0 \text{ or } H \tag{7}$$

and

$$\sigma_{ij} = 0, \quad \gamma_{ij} = 0 \quad (i, j = 1, 2). \tag{8}$$

2.2. *Fluid motion*

The non-dimensional governing equations for an incompressible fluid flow are

$$\frac{\partial \boldsymbol{u}}{\partial t} + \boldsymbol{u} \cdot \nabla \boldsymbol{u} = -\nabla p + \frac{1}{Re} \nabla^2 \boldsymbol{u} + \boldsymbol{f}, \tag{9}$$

$$\nabla \cdot \boldsymbol{u} = 0. \tag{10}$$

Here, $\boldsymbol{u} = (u, v, w)$ is the velocity vector, p is the pressure, $Re = \rho_0 U_\infty L/\mu$ is the Reynolds number, where ρ_0 is the fluid density and μ is the dynamic viscosity, and $\boldsymbol{f}$ is the momentum forcing applied to enforce the no-slip boundary condition on the flag. Note that different characteristic densities ρ_0 and ρ_1 are used in the non-dimensionalization of (9) and (4), respectively. In (9), the momentum forcing $\boldsymbol{f}$ is

scaled by $\rho_0 U_\infty^2/L$, while in (4) the Lagrangian counterpart $\boldsymbol{F}$ is scaled by $\rho_1 U_\infty^2/L$. This difference should be taken into consideration when transforming between the Lagrangian and Eulerian momentum forcings.

2.3. *Fluid–flag interaction*

The immersed boundary method of Huang & Sung (2009) is adopted to deal with the fluid–flag interaction. In the proposed method, two sets of Lagrangian point are used: one is the structure position $\boldsymbol{X}$ obtained from the flag motion equation, and the other is the corresponding IB point $\boldsymbol{X}_{ib}$ which moves with the local fluid velocity $\boldsymbol{U}_{ib}$, i.e.

$$\boldsymbol{X}_{ib}^{n+1} = \boldsymbol{X}_{ib}^{n} + \boldsymbol{U}_{ib}^{n+1}\Delta t, \tag{11}$$

where the superscript n denotes the nth time step. To calculate $\boldsymbol{U}_{ib}$, an interpolation of the fluid velocity onto the structure position $\boldsymbol{X}$ is performed:

$$\boldsymbol{U}_{ib}(s_1, s_2, t) = \int_\Omega \boldsymbol{u}(\boldsymbol{x}, t)\delta(\boldsymbol{X}(s_1, s_2, t) - x)\,\mathrm{d}\boldsymbol{x}, \tag{12}$$

where δ denotes the Dirac delta function (Peskin 2002). To enforce the no-slip condition along the fluid–structure interface, the momentum forcing in (4) is formulated as follows:

$$\boldsymbol{F}^n = -\kappa\left(\tilde{\boldsymbol{X}}_{ib}^{n+1} - 2\boldsymbol{X}^n + \boldsymbol{X}^{n-1}\right), \tag{13}$$

where κ is a large constant, and $\tilde{\boldsymbol{X}}_{ib}^{n+1}$ is an estimation of the new position of the IB point, i.e.

$$\tilde{\boldsymbol{X}}_{ib}^{n+1} = \boldsymbol{X}_{ib}^{n} + \boldsymbol{U}_{ib}^{n}\Delta t. \tag{14}$$

Note that the right-hand side of (13) is actually a discretization of the inertial force term in (4) but differs by a multiplicative factor. Thus, (13) can be regarded as a result of the flag motion equation by neglecting the elastic force term and multiplying a relaxation factor. Essentially, it works as a feedback law as proposed by Goldstein (1993). Replacing the unknown flag position at the next time step with an estimation of the new position of the IB point enforces the flag to move with the local fluid velocity.

Then the Lagrangian momentum forcing term is transformed into the Eulerian form by also using the Dirac delta function:

$$\boldsymbol{f}(\boldsymbol{x}, t) = \rho \int_\Gamma \boldsymbol{F}(s_1, s_2, t)\delta(\boldsymbol{x} - \boldsymbol{X}(s_1, s_2, t))\,\mathrm{d}s_1\,\mathrm{d}s_2, \tag{15}$$

where $\rho = \rho_1/(\rho_0 L)$ denotes the mass ratio, which comes from the non-dimensionalization. Note the fact that the Dirac delta function is three-dimensional but there are only two integrals, $\mathrm{d}s_1$ and $\mathrm{d}s_2$, in (15), which indicates a jump in fluid pressure across the flag.

2.4. *Numerical method*

The discretized form of the flag motion equation (4) is written as

$$\frac{\boldsymbol{X}^{n+1} - 2\boldsymbol{X}^n + \boldsymbol{X}^{n-1}}{\Delta t^2} = K\boldsymbol{X}^{n+1} + Fr\frac{\boldsymbol{g}}{g} - \boldsymbol{F}^n + \boldsymbol{BC}, \tag{16}$$

where K represents the discrete operator of the elastic force term (cf. Appendix B), and $\boldsymbol{BC}$ is the boundary condition vector which contains the known positions at the fixed boundary. After rearrangement, (16) becomes

$$\boldsymbol{A}\boldsymbol{X}^{n+1} = \boldsymbol{R}^n. \tag{17}$$

Here $\boldsymbol{A} = \boldsymbol{I} - \Delta t^2 K$, where $\boldsymbol{I}$ is the unit matrix of size $M(N+1)$ and $\boldsymbol{R}^n \equiv \boldsymbol{X}^n + \Delta t \boldsymbol{U}^n + \Delta t^2 Fr \cdot \boldsymbol{g}/g - \Delta t^2 \boldsymbol{F}^n + \Delta t^2 \boldsymbol{BC}$ by applying $\boldsymbol{U}^n = (\boldsymbol{X}^n - \boldsymbol{X}^{n-1})/\Delta t$. We found that symmetry and positive definiteness of the matrix $\boldsymbol{A}$ are preserved in this study. Hence, the conjugate gradient method can be utilized to solve (17) in an efficient manner due to its fast convergence rate.

On the other hand, a fractional step method is adopted to solve the discretized Navier–Stokes equations (Kim, Baek & Sung 2002), which can be written as,

$$\frac{\boldsymbol{u}^{n+1} - \boldsymbol{u}^n}{\Delta t} + N\boldsymbol{u}^{n+1} = -Gp^{n+1/2} + \frac{1}{2Re}(L\boldsymbol{u}^{n+1} + L\boldsymbol{u}^n) + \boldsymbol{f}^n + \boldsymbol{mbc}, \tag{18}$$

$$D\boldsymbol{u}^{n+1} = 0 + cbc, \tag{19}$$

where N, G, L and D are the linearized discrete convective operator, the discrete gradient operator, the discrete Laplacian operator and the discrete divergence operator, respectively. The velocity boundary conditions for the momentum equations and the continuity equation have been imposed on $\boldsymbol{mbc}$ and cbc, respectively. The momentum forcing term $\boldsymbol{f}^n$ is calculated using (15), which is discretized as

$$\boldsymbol{f}^n = \rho \sum_{i=0}^{M} \sum_{j=0}^{N} \boldsymbol{F}_{i,j}^n \delta_h \left(\boldsymbol{x} - \boldsymbol{X}_{i,j}^n \right) \Delta s_1 \Delta s_2, \quad \forall \boldsymbol{x} \in g_h, \tag{20}$$

where $\delta_h(\boldsymbol{x}) = \phi(x/h)\phi(y/h)\phi(z/h)/h^3$ with ϕ the four-point smoothed approximation of the delta function (Peskin 2002), and g_h is its support. Here h denotes the mesh size; in the present simulations a mesh of uniform size is distributed around the IB, i.e. $h = \Delta x = \Delta y = \Delta z$. After obtaining the fluid velocity field, we use the smoothed delta function to interpolate the fluid velocity on the flag as dictated in (12),

$$\boldsymbol{U}_{ib}^{n+1} = \sum_{x \in g_h} \boldsymbol{u}^{n+1} \delta_h(\boldsymbol{X} - \boldsymbol{x}) h^3. \tag{21}$$

The overall process for simulating flag motion in a uniform flow at each time step is briefly summarized as follows: (i) calculate the Lagrangian momentum forcing $\boldsymbol{F}^n$ using (13) and spread it to the Eulerian grid using (20); (ii) solve (18) and (19) to obtain updated fluid velocity field and pressure field, and calculate the new position of the IB point using (11); (iii) solve (17) to obtain the flag position at the new time step. In the present method, the Eulerian fluid motion and the Lagrangian flag motion are solved independently. In this way, the massive boundary can be handled in an efficient manner with retention of the use of the fast Fourier transform (FFT) method. More details of the present numerical method can be found in Huang & Sung (2009), where the solver was verified using several numerical examples. Moreover, validations of the filament simulation as a two-dimensional flag problem were provided in Huang *et al.* (2007).

3. Results and discussion

In the present simulations, the computational domain for fluid flow is a rectangular box, extending from $(-1, -4, -1)$ to (7, 4, 1) in the streamwise (x), transverse (y) and spanwise (z) directions, respectively. Here the domain sizes are scaled by the flag length L. Dirichlet boundary conditions ($u = U_\infty$, $v = 0$, $w = 0$) are used at the inflow ($x = -1$) and far-field boundaries ($y = \pm 4$), a convective boundary condition ($\partial \boldsymbol{u}/\partial t + U_C \partial \boldsymbol{u}/\partial x = 0$) is used at the outflow ($x = 7$) and periodic boundary conditions are used in the spanwise direction. A grid size of $513 \times 151 \times 129$ is used to discretize the computational domain. The grid is uniformly distributed along the x- and z-axis,

while stretched in the y-axis. The fixed boundary of the flag ($s_1 = 0$) is aligned with the z-axis, with its midpoint ($s_1 = 0$, $s_2 = H/2$) coinciding with the origin of the Eulerian coordinate system, as shown in figure 1. The flag is discretized by a uniform mesh $\Delta s_1 = \Delta s_2 = 1/64$, which is equivalent to the Eulerian grid spacings Δx, Δy and Δz near the IB. The flag is initially held at an angle of $a = 0.1\pi$ from the xz plane, as expressed by,

$$\boldsymbol{X}(s_1, s_2, t = 0) = (s_1 \cos a, s_1 \sin a, s_2 - H/2)\,. \tag{22}$$

In the following simulations, the parameters of $L = 1.0$, $H = 1.0$, $\rho = 1.0$, $\phi_{11} = \phi_{22} = 10^3$, $\phi_{12} = 10$, $\gamma_{11} = \gamma_{22} = \gamma_{12} = 0.0001$ are used for the flag by default unless otherwise stated. Gravity is first neglected in our simulations for the results presented in §§ 3.1–3.3, i.e. $Fr = 0$, while a flag flapping under gravity is specifically shown in § 3.4. The free constant in calculating the Lagrangian force by (13) is set to $\kappa = 10^5$, and a time step of $\Delta t = 0.0003$ is used, which were chosen to ensure that the results are converged.

3.1. *Three-dimensional flapping motion*

Figure 2 shows time histories of the streamwise, transverse and spanwise displacements of points A, B and C on the trailing edge of the flag (figure 1) from their equilibrium positions at three Reynolds numbers, i.e. $Re = 100$, 200 and 500. Correspondingly, the instantaneous flag positions are shown in figure 3 at four time instants as labelled in figure 2. The trailing edge reaches its maximum transverse position at the instants 1 and 3, while moving across the equilibrium position ($y = 0$) at the instants 2 and 4. A longitudinal travelling wave is seen in the time series of instantaneous flag positions.

At $Re = 100$ (figure 2*a*), the streamwise and transverse displacements (X' and Y' respectively) of the mid-point B have larger amplitudes than those of the corner points A and C, indicating that the flag is bended along the spanwise direction as directly seen in figure 3(*a*). Since the longitudinal travelling wave flattens the deformation in the spanwise direction, the bending of the flag is only apparent close to the two corners on the trailing edge. Interestingly, the difference of X' and Y' between the mid-point and the corner points becomes smaller at $Re = 200$ (see figure 2*b*), and the trailing edge is less bended (see figure 3*b*). The reason is that the viscous force of fluid is increased as the Reynolds number decreases, and meanwhile the pressure difference across the flag is reduced more significantly near the side edges. The bending extent of the trailing edge is more clearly measured by checking the amplitude of the spanwise displacement (Z') of the corner points (figures 2*a* and 2*b*), which is smaller at $Re = 200$. Another observation on figure 2 shows that X' and Z' do not reach their maximum positions at the instants 1 and 3 as Y', mainly due to the longitudinal travelling wave on the flag.

Figure 4 shows a top view (in xy plane) of superposition of the longitudinal curves passing points A, B and C. For $Re = 100$ and 200 (see figures 4*a* and 4*b* respectively), the result of point A (left) is identical to that of point C (right), but the result of point B (middle) shows a bigger '∞' trajectory of the free end, which is formed by the flapping of the flag with the longitudinal travelling wave and is more inhibited at the side edges than the centre region. The '∞' trajectory of point C can also be seen clearly in figure 5, which shows the phase relation of the transverse position (Y) and the streamwise and spanwise positions (X and Z respectively). Due to the bending of the trailing edge, the YZ-phase relation also shows a '∞' trajectory at $Re = 100$ (figure 5*a*), while becoming a double '∞' trajectory at $Re = 200$ (figure 5*b*), indicating that the wavenumber is increased along the spanwise direction on the flag as the Reynolds number increases.

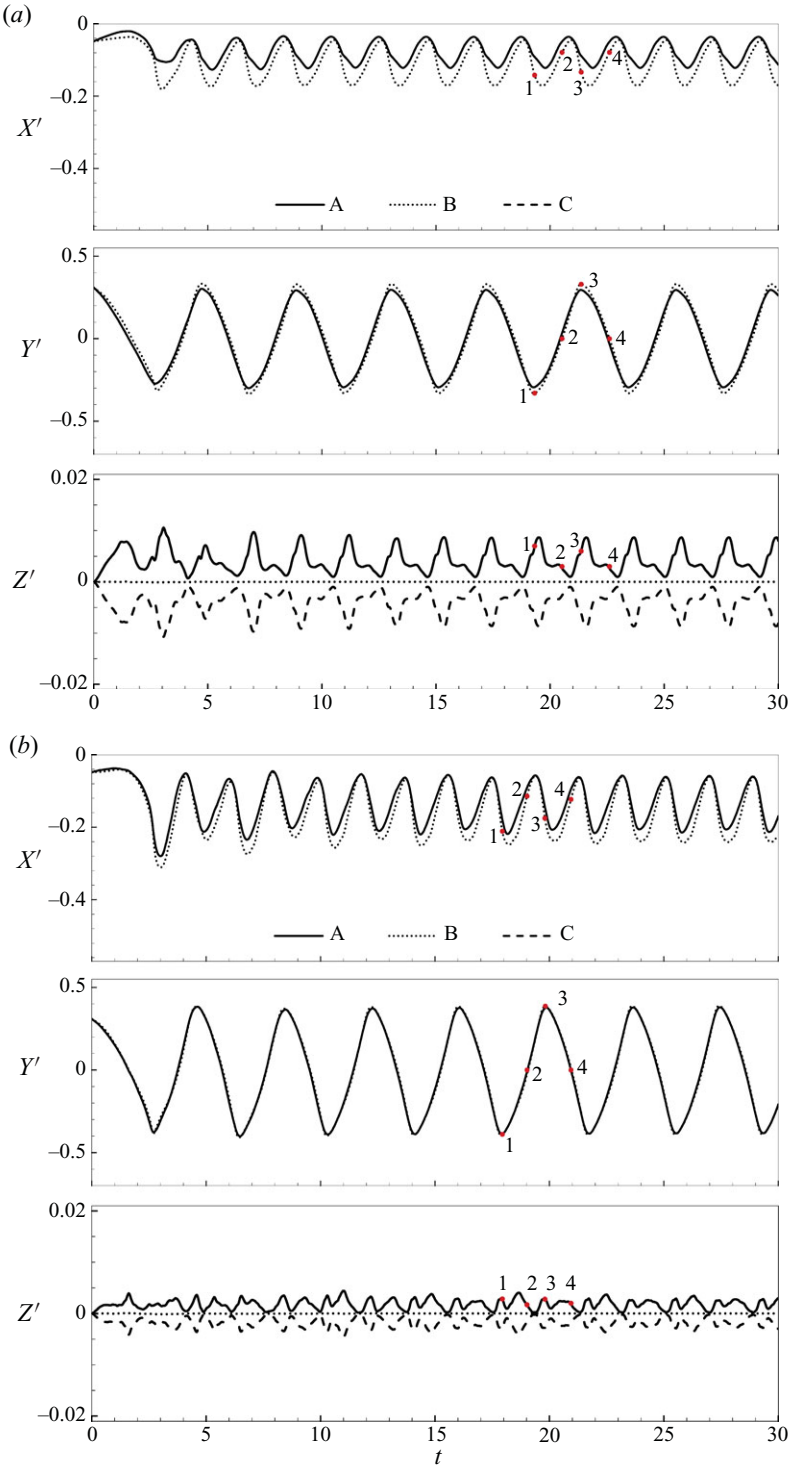

FIGURE 2. For caption see next page.

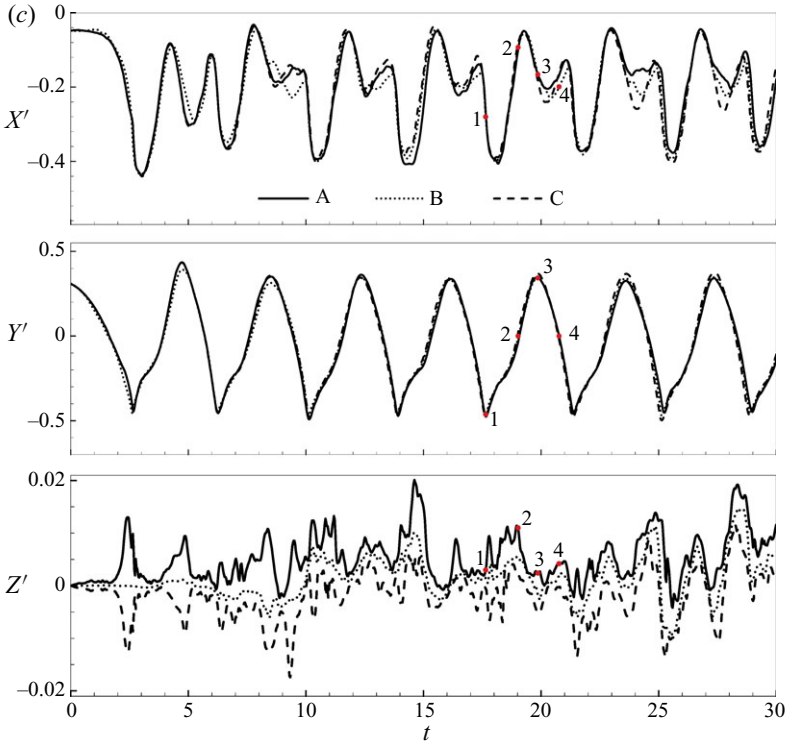

FIGURE 2. Time histories of the streamwise, transverse and spanwise displacements of points A, B and C (figure 1) from their equilibrium positions: (*a*) $Re = 100$; (*b*) $Re = 200$; (*c*) $Re = 500$. Points 1, 2, 3 and 4 correspond sequentially to the four instants adopted in figure 3.

When the Reynolds number is increased to $Re = 500$, the flapping motion becomes more complicated as seen in figure 2(*c*). The time history of X' shows that two waves are superposed unlike the cases at $Re = 100$ and 200, where only a single wave is observed. As a result, the flapping is asymmetric in the y direction, as shown in figures 4(*c*) and 5(*c*). To see more clearly, the snapshots of the centreline passing point B with a time interval of 0.3 are plotted in figure 6 for $Re = 500$. During the first-half period (figure 6*a*), the flag is moving leftwards and a wave is travelling towards the free end. However, a wave is travelling backwards to the fixed end as the flag moves rightwards during the second-half period (figure 6*b*). The backward travelling wave is formed by reflection at the free end and is sustained under the condition that the flag inertia overwhelms the viscous force of the surrounding fluid. At $Re = 100$ and 200, the backward travelling wave is just damped by the fluid viscosity and is swept downstream. Note that the formation of the backward travelling wave is also related to the initial position of the flag.

Another effect of the increasing Reynolds number is the appearance of asymmetry of the flag about its centreline ($s_2 = H/2$), as shown by the spanwise displacement (figure 2*c*). Furthermore, small-scale wave motions are generated on the flag (figure 3*c*) and the YZ-phase relation of point C shows an irregular pattern (figure 5*c*). We use the average spanwise position of points A and C to measure the asymmetry of the flag, i.e. $\varepsilon_Z = |Z_A + Z_C|$. Figure 7 shows time histories of ε_Z at different Reynolds numbers. Given a uniform initial flow field (figure 7*a*), ε_Z remains at a very low level for $Re = 100$ and 200, while grows exponentially for $Re = 500$. Hence, the appearance

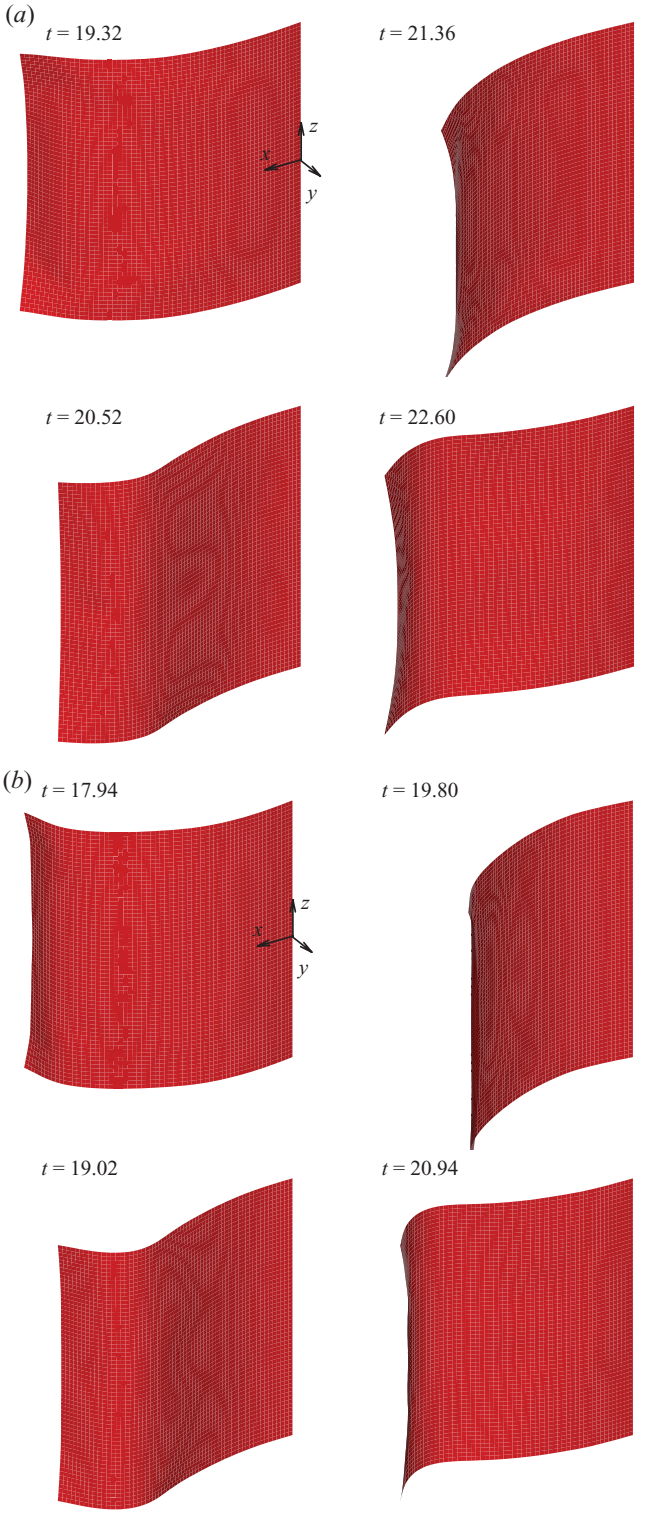

FIGURE 3. (Colour online) For caption see next page.

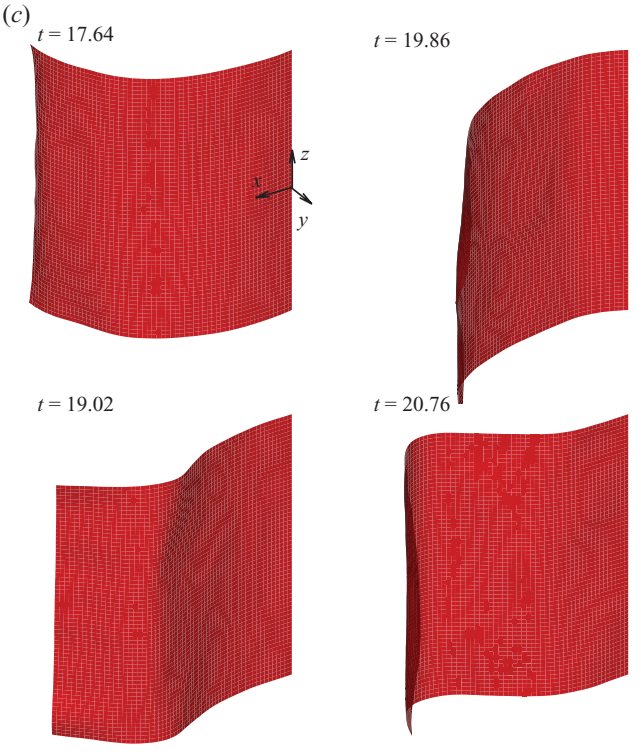

FIGURE 3. (Colour online) Instantaneous positions of a flapping flag at the four instants as labelled in figure 2: (*a*) $Re = 100$; (*b*) $Re = 200$; (*c*) $Re = 500$. Supplementary movie 1 available at journals.cambridge.org/flm.

of asymmetry is a result of the coupled fluid–flag instability. To confirm the status of symmetry at each Reynolds number, an initial random perturbation is added to the uniform flow. As shown in figure 7(*b*), ε_Z decreases gradually for $Re = 100$ and 200, while increases until saturated for $Re = 500$, indicating that the symmetry of flag is stable for $Re = 100$ and 200, but unstable for $Re = 500$. Moreover, a flag of different width is also simulated for comparison. Figure 8 shows time histories of $\varepsilon_Z = |Z_A + Z_C|$ for $H = 1.0$ and 1.5. Both cases have a symmetric solution at $Re = 100$ (figure 8*a*), while the magnitude of ε_Z is larger for $H = 1.5$. When the Reynolds number is increased to 500 (figure 8*b*), the asymmetry develops gradually until saturated in both cases, and the growth rate of ε_Z is increased as H increases.

3.2. *Three-dimensional wake structures*

Figure 9 shows vortical structures shed from the flag of $H = 1.0$ at the minimum transverse position, corresponding to the instant 1 labelled in figure 2, for $Re = 100$, 200 and 500. Here the λ_2 criterion (Jeong & Hussain 1995) is used to identify the vortical structures and an isovalue of $\lambda_2 = -0.2$ is chosen to plot the three-dimensional contours. Moreover, the pressure contours in the xy plane of $z = -0.5$, 0 and 0.5 at each Reynolds number are displayed in figure 10, where the flag side edges and centreline are also plotted. Note that the flag side edges are not located in the planes in general due to the spanwise bending of the flag, but the deviation is small.

At $Re = 100$ (figure 9*a*), two vortical structures are formed by each flapping motion of the side edges, which are directed mainly in the longitudinal direction and symmetric

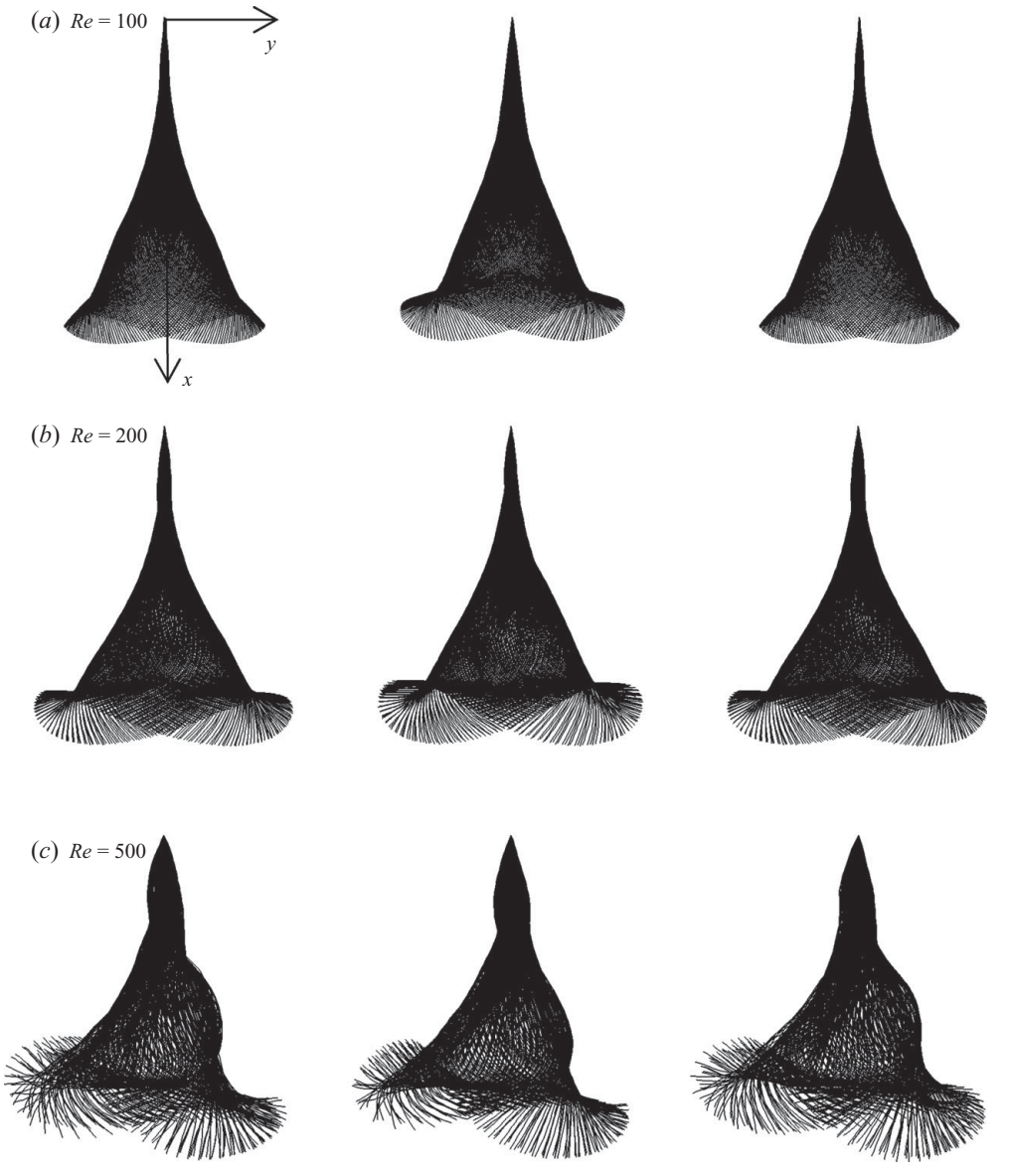

FIGURE 4. Top view of superposition of the longitudinal curves passing points A (left), B (middle) and C (right) as marked in figure 1: (*a*) $Re = 100$; (*b*) $Re = 200$; (*c*) $Re = 500$.

about the flag centreline. On the other hand, the vortical structure shed from the trailing edge is relatively weak. As shown in figure 10(*a*), the pressure difference across the flag is strong at the centre region, while the positive pressure is significantly decreased near the side edges due to the vortex shedding. This may explain the bending of the trailing edge (figure 3*a*) and the additional damping of the travelling wave along the side edges (figure 4*a*). At $Re = 200$ (figure 9*b*), the vortical structure shed from the trailing edge becomes stronger and connects those from the side edges to form a 'hairpin' structure with two antennae, which is still symmetric about the flag centreline. The pressure difference is also increased as the Reynolds number increases as seen in figure 10(*b*), and so does the positive pressure near the side edges

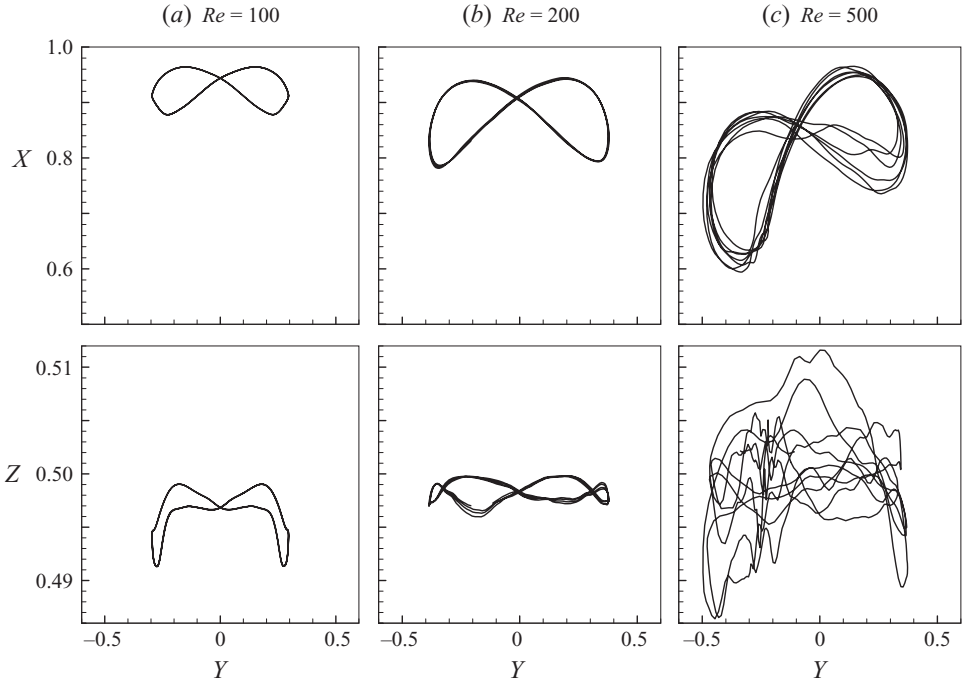

FIGURE 5. Phase relation of the transverse position and the streamwise and spanwise positions of point C (figure 1): (*a*) $Re = 100$; (*b*) $Re = 200$; (*c*) $Re = 500$.

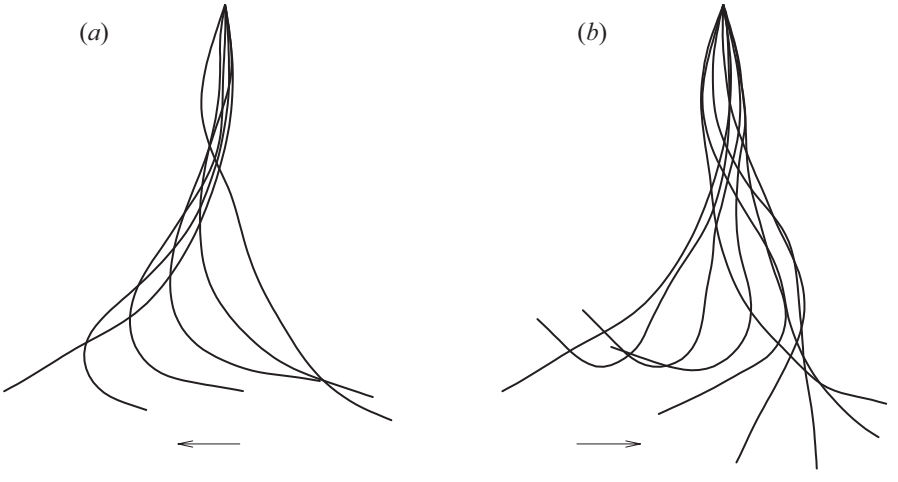

FIGURE 6. Snapshots of the centreline passing point B (figure 1) at $Re = 500$ during (*a*) the first-half period and (*b*) the second-half period.

as compared with that at $Re = 100$. The increase of the pressure difference together with the reduction of the viscous force causes the trailing edge to be bended to a less extent (figure 3*b*). At $Re = 500$ (figure 9*c*), O-shaped vortical structures are shed from the flag and some thin elongated vortical structures are formed by stretching between the O-shaped structures. Meanwhile, the pressure difference becomes much stronger in the centre region and near the side edges as well, and an asymmetry between the

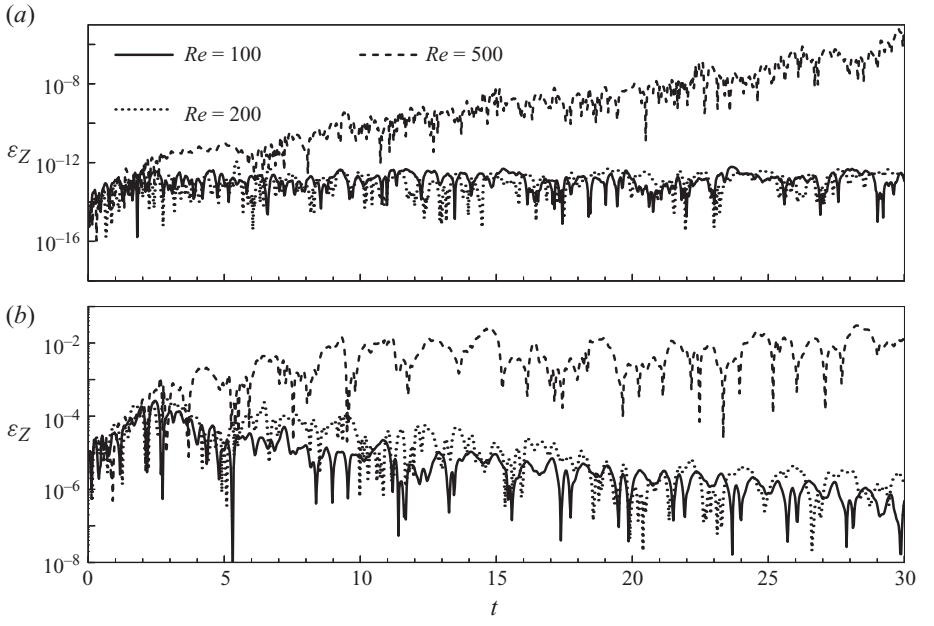

FIGURE 7. Time histories of the difference of the spanwise position between points A and C (figure 1): (*a*) without initial perturbation; (*b*) with initial perturbation.

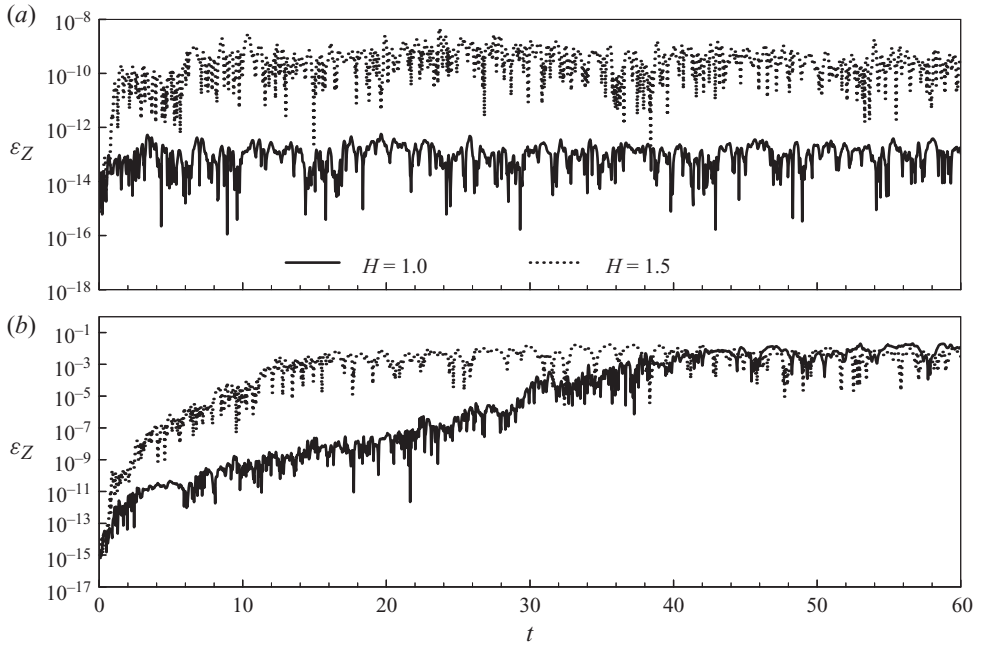

FIGURE 8. Time histories of the difference of the spanwise position between points A and C (figure 1) for $H = 1.0$ and 1.5 without initial perturbation: (*a*) $Re = 100$; (*b*) $Re = 500$.

xy planes of $z = -0.5$ and 0.5 can be seen in figure 10(*c*). From figure 9 we can see a significant difference of the vortical structures in the wake of the flag between the present results and the two-dimensional simulations (Connell & Yue 2007; Huang *et al.* 2007). Due to the formation of the structures at the flag side edges, the vortical

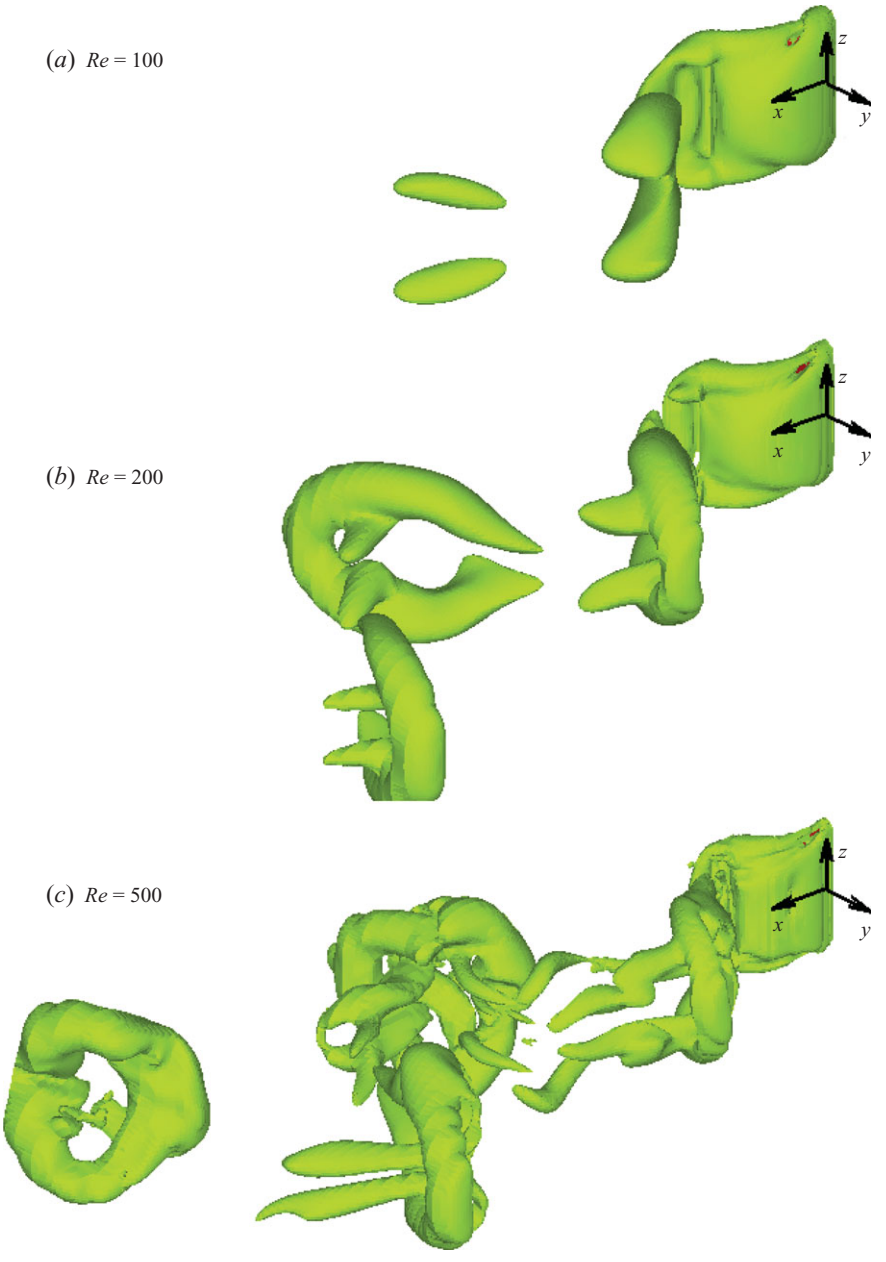

FIGURE 9. (Colour online) Vortical structures shedding from the flapping flag of $H = 1.0$ at instant 1 as labelled in figure 2: (*a*) $Re = 100$; (*b*) $Re = 200$; (*c*) $Re = 500$. Supplementary movie 2 available at journals.cambridge.org/flm.

structures shed from the trailing edge are attenuated and the pressure difference across the flag is reduced, as compared with the two-dimensional case. As a result, the flag is stabilized by the effect of side edges.

To see more clearly the fluid motion in the wake of the flapping flag, we add some tracing particles which follow the local fluid velocity but not conversely modify the fluid motion. The particles are released at $(-0.5, \pm 0.2, \pm 0.3)$ with a time interval of

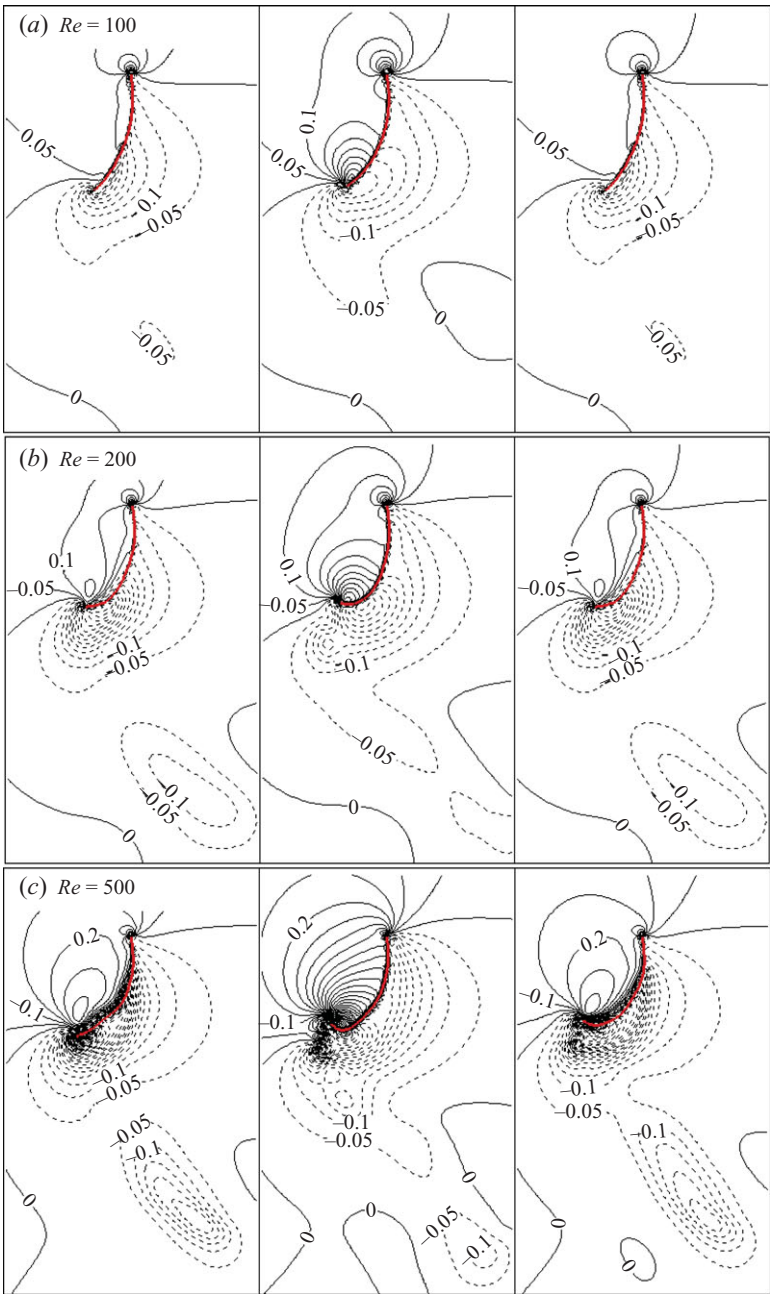

FIGURE 10. (Colour online) Pressure contours near the flag in the xy plane of $z = -0.5$ (left), 0 (middle) and 0.5 (right) at the instant when the trailing edge reaches the minimum transverse position: (*a*) $Re = 100$; (*b*) $Re = 200$; (*c*) $Re = 500$.

0.05 from $t = 0$. Snapshots of the tracing particles at the instant 1 (figure 2) from both side view and top view are shown in figure 11. Spiral motions are formed by the rows of particles from both sides of the flag for the three cases, i.e. $Re = 100$, 200 and 500. The particles close to the trailing edge are pushed towards the side edges, and consequently the trailing edge is bended to some extent, which has a stabilization

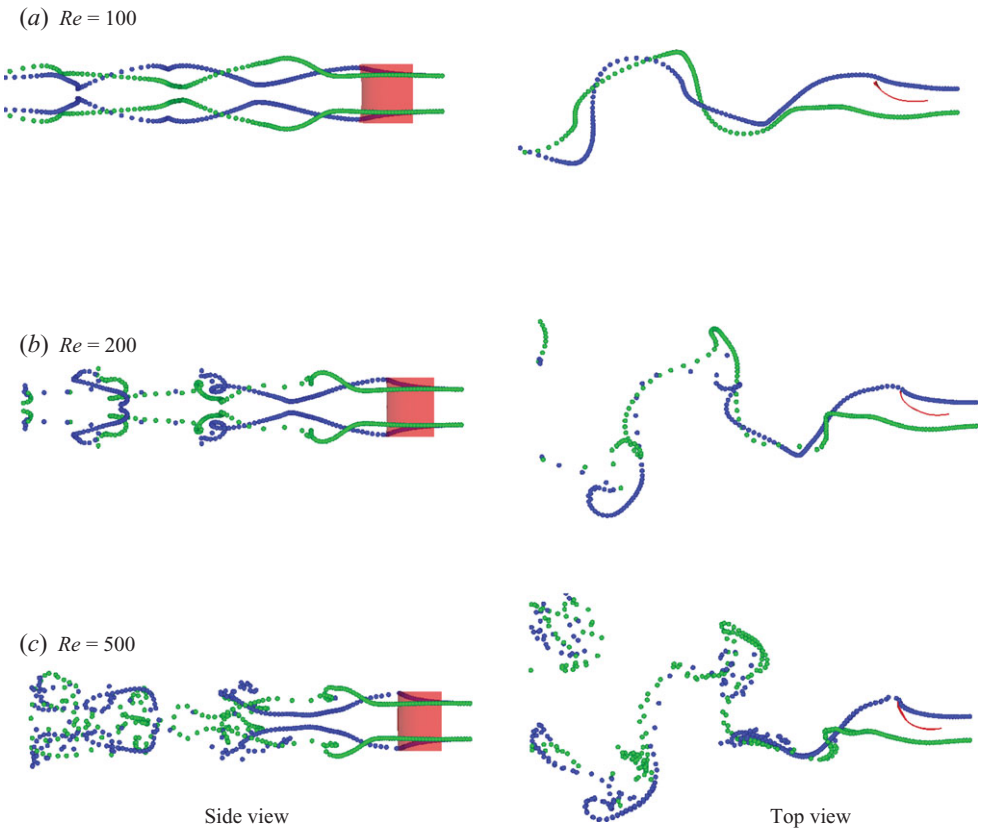

FIGURE 11. (Colour online) Snapshots of tracing particles at instant 1 as labelled in figure 3, which are released at $(-0.5, \pm 0.2, \pm 0.3)$ with a time interval of 0.05: (*a*) $Re = 100$; (*b*) $Re = 200$; (*c*) $Re = 500$. Supplementary movie 3 available at journals.cambridge.org/flm.

effect on the flag. The rolling motion in the spanwise direction is intensified as the Reynolds number increases. At $Re = 500$ (figure 11*c*), the flag interacts with the fluid strongly at the trailing edge and causes a rapid acceleration of the fluid as can be seen from large spacings of the particles near the trailing edge. This accounts for the loss of symmetry of the fluid as well as the flag about its centreline as presented in the previous section.

Similarly, the instantaneous vortical structures shed from the flag of $H = 0.5$ at the minimum transverse position are shown in figure 12. Comparing with the case of $H = 1.0$ (figure 9), the strength of vortical structures is weakened for $H = 0.5$. As the flag width decreases, the pressure difference across the flag is reduced due to the three-dimensional vortex shedding, and so does the flapping amplitude, which can be seen by comparing figure 13(*a*) with figure 10(*c*). Furthermore, we increase the flag density to $\rho = 2.0$ for the flag of $H = 0.5$, and the instantaneous vortical structures are displayed in figure 14. The vortical structures becomes stronger but the frequency is decreased as compared with the case of $H = 0.5$ and $\rho = 1.0$. Since the vortex shedding causes the decrease of the pressure difference across the flag, the pressure difference of the case of $H = 0.5$ and $\rho = 2.0$ is not as strong as that of $H = 1.0$ and $\rho = 1.0$ by comparing figure 13(*b*) with figure 10(*c*). As the flag density increases, however, a vortex procession is generated behind a flag at $Re = 500$ as shown in

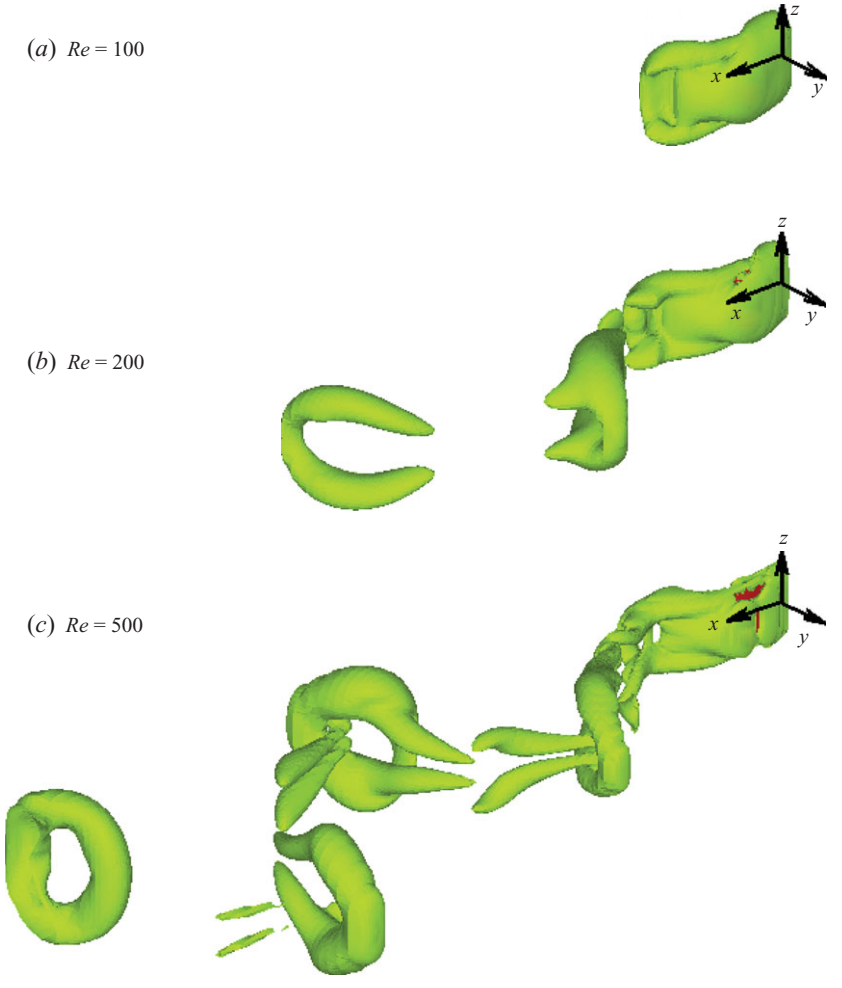

FIGURE 12. (Colour online) Vortical structures shedding from the flapping flag of $H = 0.5$ and $\rho = 1.0$ at the instant when the trailing edge reaches the minimum transverse position: (*a*) $Re = 100$; (*b*) $Re = 200$; (*c*) $Re = 500$. Supplementary movie 4 available at journals.cambridge.org/flm.

figure 14(*c*). This procession can be seen more clearly in the corresponding animation available online, which is different from the cases of $\rho = 1.0$ where a pair of alternative vortical structures is shed during each flapping period. Such vortex procession was also observed behind the two-dimensional flag model by visualizations of a flowing soap film (Zhang *et al.* 2000) and by two-dimensional simulations (Huang *et al.* 2007).

3.3. *Flapping frequency*

Figure 15 shows the Strouhal number and the amplitude of flag's flapping as functions of the Reynolds number for two flag widths, i.e. $H = 0.5$ and 1.0, and three different densities, i.e. $\rho = 0.5$, 1.0 and 2.0. Two length scales can be used to define the Strouhal number: the flag length L or the flapping amplitude A measured as the average flapping span. Specifically, they are expressed respectively as,

$$St = \frac{fL}{U_\infty} \quad \text{and} \quad St' = \frac{fA}{U_\infty}, \tag{23}$$

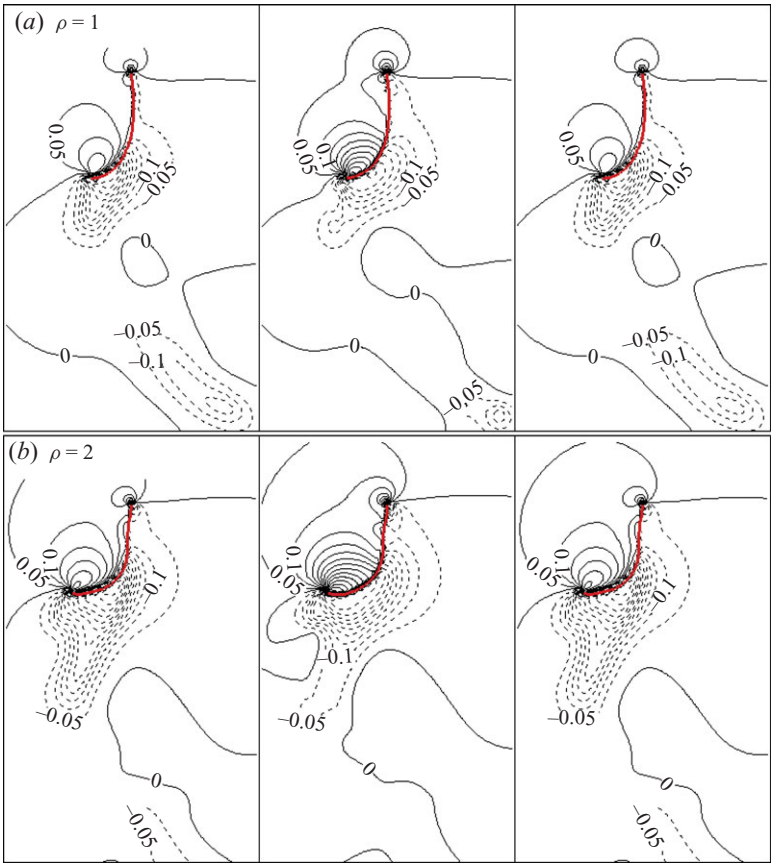

FIGURE 13. (Colour online) Pressure contours near the flag in the xy plane of $z = -0.25$ (left), 0 (middle) and 0.25 (right) at the instant when the trailing edge reaches the minimum transverse position for $H = 0.5$ and $Re = 500$: (*a*) $\rho = 1.0$; (*b*) $\rho = 2.0$.

where f denotes the flapping frequency. As shown in figures 15(*a*) and 15(*b*), St remains constant for each case while A is increased slightly as the Reynolds number increases, which is consistent with the experimental observation of Shelley *et al.* (2005). The lack of variation in St and A with the Reynolds number indicates that the flag inertia dominates over the viscous force exerted on the flag by the surrounding fluid. Interestingly, St' collapses for different ρ to the value around 0.2, while the difference between $H = 0.5$ and $H = 1.0$ is not diminished, as seen in figure 15(*c*).

Variations of St, St' and A with ρ and H can be seen more clearly in figures 16 and 17, respectively. As ρ increases (figure 16), St is decreased while A is increased. As a result, St' is only slightly varied with ρ. If neglecting the three-dimensional effect, a qualitative analysis for small-amplitude motion (Argentina & Mahadevan 2005) shows that the flag inertia scales as $\rho_1 f^2 H A$, while the pressure difference across the flag scales as $\rho_0 U_\infty^2 H A/L$. Equating the above two forces yields

$$f \sim \left(\rho_0 U_\infty^2 / \rho_1 L\right)^{1/2} \quad \text{or} \quad St \sim \rho^{-1/2}. \tag{24}$$

The second relationship of (24) is clearly seen in figure 16(*a*), although the small–amplitude assumption is no longer valid in the present three-dimensional simulations. On the other hand, A is increased as f is decreased to maintain the circulation for

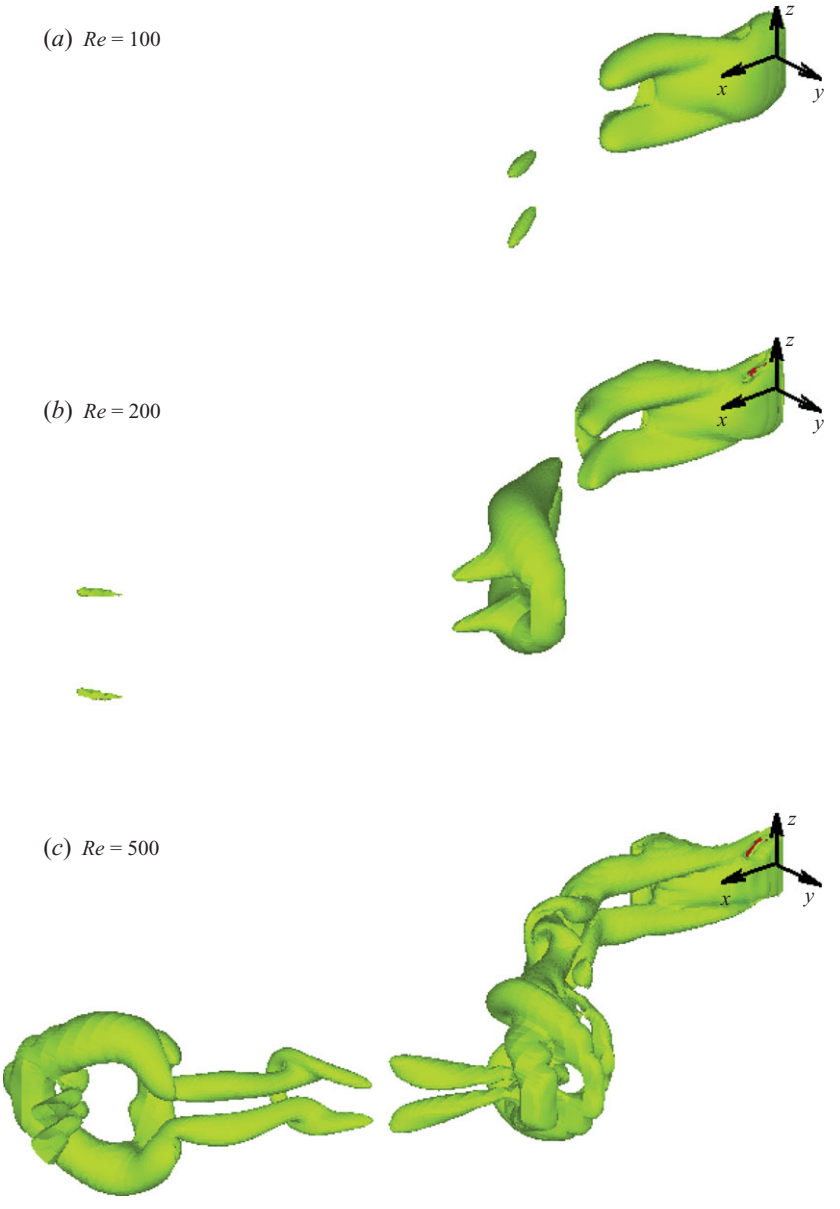

FIGURE 14. (Colour online) Vortical structures shedding from the flapping flag of $H = 0.5$ and $\rho = 2.0$ at the instant when the trailing edge reaches the minimum transverse position: (*a*) $Re = 100$; (*b*) $Re = 200$; (*c*) $Re = 500$. Supplementary movie 5 available at journals.cambridge.org/flm.

vortex shedding (Williamson 1996). Moreover, the corresponding two-dimensional computational results are also included for comparison. Some difference is seen between the two- and three-dimensional ($H = 1.0$) results, and it becomes smaller as ρ increases. It is also noted that a crossover occurs in figure 16(*b*) due to the fact that a chaotic state happens for the two-dimensional case when ρ is smaller than 1.0 but is not too small (results not shown here). The effect of the flag width is then presented in figure 17 for $\rho = 1.0$ and 4.0. As H increases, St is almost constant while A is increased

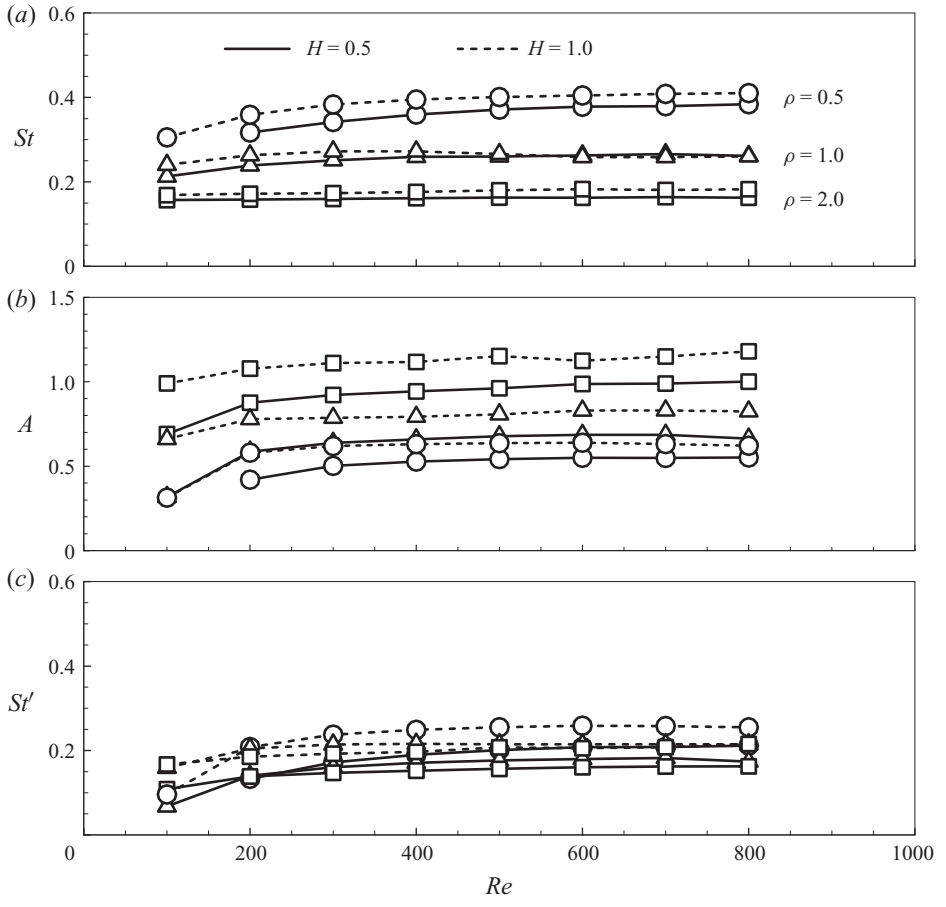

FIGURE 15. Variations of (*a*) *St*, (*b*) *A* and (*c*) St' with *Re*.

at small *H*, so St' is also increased but still remains close to 0.2. The fact that *St* is slightly varied with *H* indicates that (24) is valid by neglecting the three-dimensional effect for the range of flag width considered here. However, the increase of *A* with *H* is due to the increase of the pressure difference across the flag as shown in § 3.2, indicating that the three-dimensional effect is more significant at small *H*. Figure 17 also shows that for $\rho = 1.0$ the values are not converged to the corresponding two-dimensional results, except that *A* is matched at the crossover as seen in figure 16(*b*). However, the convergence behaviour is improved for $\rho = 4.0$. One possible reason for the difference between the two- and three-dimensional results is that the ratio of the flag width to the typical mode wavelength is not large enough at $\rho = 1$ for the two-dimensional assumption to be valid, and this ratio is increased as ρ increases (Eloy *et al.* 2008).

The range of St' in the present simulations is close to that of $0.22 \sim 0.31$ as reported by Shelley *et al.* (2005). Despite of the difference in the Reynolds number, similar St' values were also obtained in two-dimensional simulations (Connell & Yue 2007) and experiments (Jia *et al.* 2007), as listed in table 1. More interestingly, Taylor *et al.* (2003) calculated the St' values of various species of birds, bats and insects in unconfined cruising flight and found that they are constrained in a narrow range $0.2 < St' < 0.4$, and Triantafyllou *et al.* (2000) showed that the St' values of swimming dolphins, sharks and bony fish fall in a similar range. In particular, the birds engaged

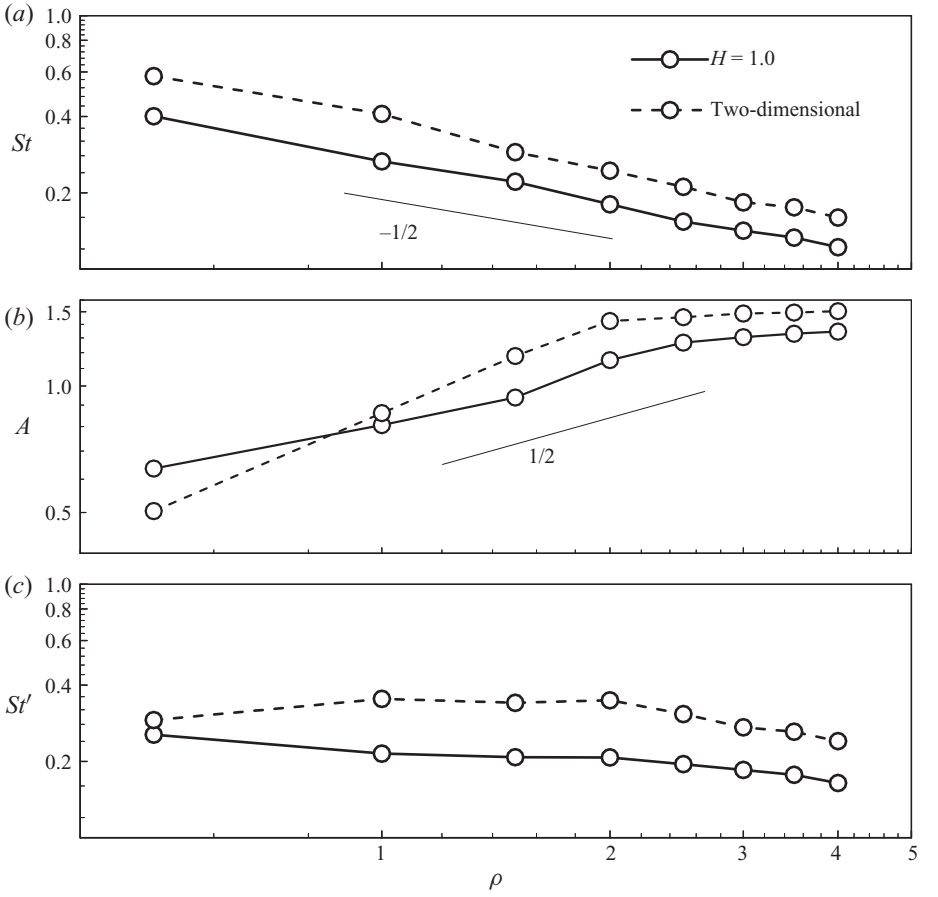

FIGURE 16. Variations of (*a*) St, (*b*) A and (*c*) St' with ρ at $Re = 500$.

in direct flight have $St' \approx 0.2$ (Taylor *et al.* 2003), which is within the range of the present results. This comparison indicates that the fluid dynamics occurring during active flying and swimming is similar to that of passive flapping, presumably to obtain high propulsive efficiency. Recall that the Strouhal number of vortex shedding from a circular cylinder ranges from 0.12 to 0.2 over a wide range of Reynolds numbers when periodic vortex shedding is established, and converges to about 0.2 after three-dimensional shedding modes are formed (Williamson 1996). Here we can see that the universal Strouhal number of the flapping flag is a result of the wake instability for the onset of vortex shedding, as proposed for the fish swimming (Triantafyllou *et al.* 2000).

3.4. *Flapping under gravity*

In this section, gravity is included in the simulation which is directed along the negative z-axis. Gravity breaks the symmetry of the flag about its centreline and causes the flag to sag down. Figure 18 shows time histories of X', Y' and Z' of points A, B and C (figure 1) for $Re = 200$, while three Froude numbers are compared, i.e. $Fr = 0.2$, 0.5 and 1.0. The instantaneous flag positions at the four instants as labelled in figure 18 are shown in figure 19, where we can see clearly the sagging of flag besides of the flapping motion in the y direction.

	Object	Method	St'
Present	Three-dimensional flapping flag of $H = 1.0$	Computation	$0.16 \sim 0.25$
Present	Three-dimensional flapping flag of $\rho = 1.0$	Computation	$0.12 \sim 0.26$
Present	Two-dimensional flapping filament	Computation	$0.25 \sim 0.35$
Taylor *et al.* (2003)	Active swimming and flying	Experiment	$0.2 \sim 0.4$
Shelley *et al.* (2005)	Three-dimensional flapping flag	Experiment	$0.22 \sim 0.31$
Connell & Yue (2007)	Two-dimensional flapping filament	Computation	$0.2 \sim 0.3$
Jia *et al.* (2007)	Two-dimensional flapping filament	Experiment	≈ 0.2
Williamson (1996)	Circular cylinder	Review	$0.12 \sim 0.2$

TABLE 1. Comparison of the Strouhal number defined in terms of flapping amplitude or cylinder diameter with that of previous studies.

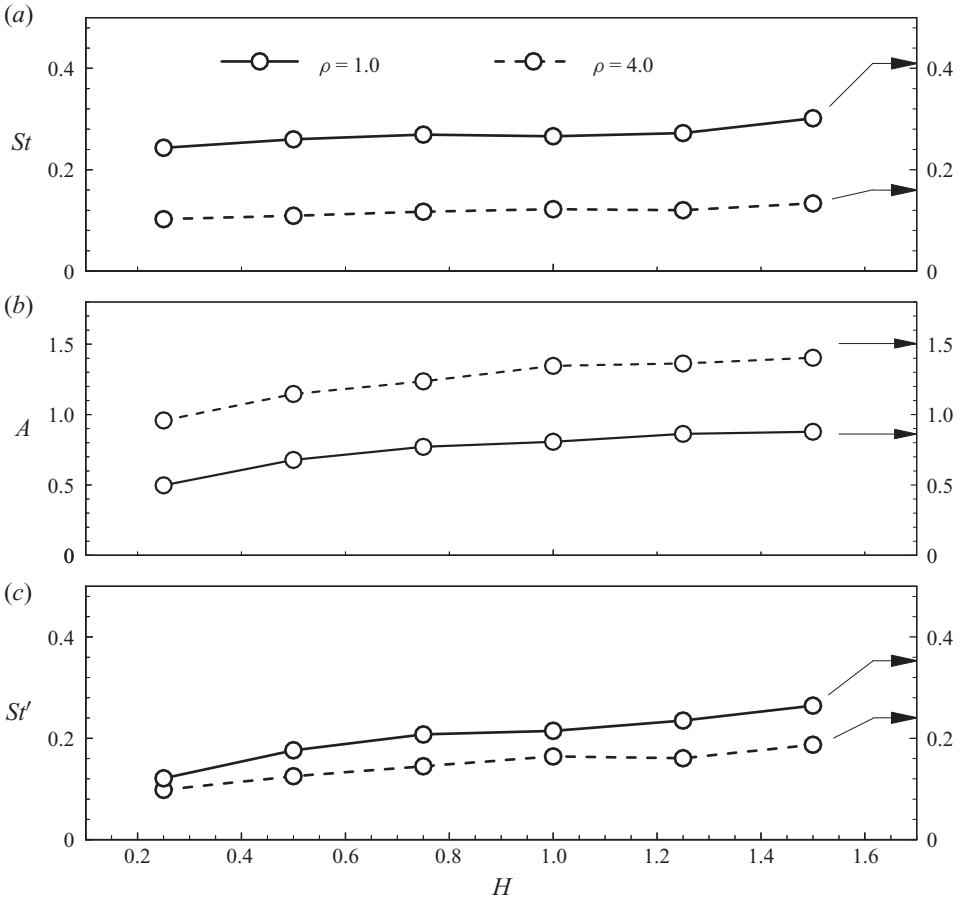

FIGURE 17. Variations of (*a*) St, (*b*) A and (*c*) St' with H at $Re = 500$. The values marked on the axes by arrows denote the corresponding two-dimensional results.

At $Fr = 0.2$ and 0.5, the flag flaps regularly in the y direction, but apparent phase difference is seen for the three points due to the sagging of flag as shown in figures 18(*a*) and 18(*b*), unlike the gravity-free cases where points A, B and C are moving almost in phase and a slight phase difference is caused by the bending of the trailing edge. Moreover, the upper corner on the trailing edge (point C) undergoes a fast rolling

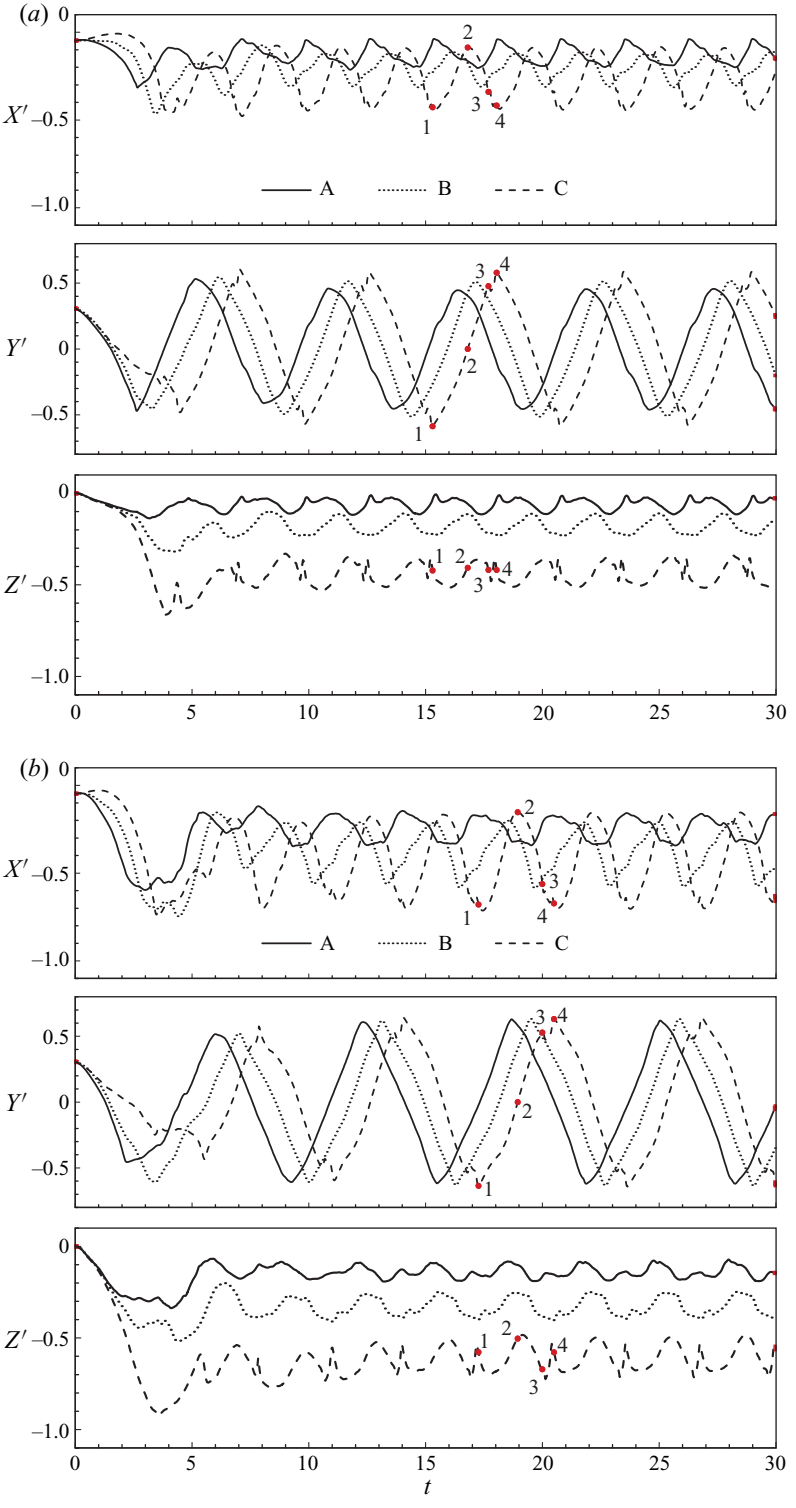

FIGURE 18. (Colour online) For caption see next page.

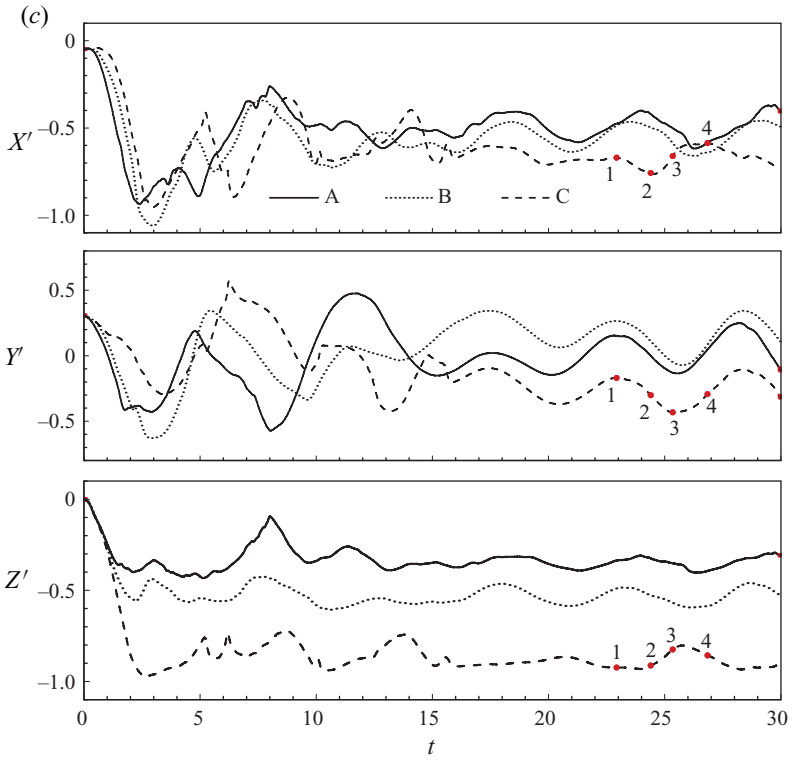

FIGURE 18. (Colour online) Time histories of the streamwise, transverse and spanwise displacements of points A, B and C (figure 1) from their equilibrium positions for $Re = 200$: (*a*) $Fr = 0.2$; (*b*) $Fr = 0.5$; (*c*) $Fr = 1.0$. Points 1, 2, 3 and 4 correspond sequentially to the four instants adopted in figure 19.

motion near the maximum (and minimum) transverse position during each flapping period, which is shown in figures 19(*a*) and 19(*b*) from instant 3 to instant 4 as well as in figures 18(*a*) and 18(*b*). Comparing with the case of $Fr = 0.2$, the amplitudes of all X', Y' and Z' are increased at $Fr = 0.5$, indicating a more energetic flapping as the Froude number increases. The absolute mean values of X' and Z' are increased at $Fr = 0.5$ since the flag is sagging to a larger extent as evident by comparing figure 19(*a*) with figure 19(*b*). Specifically, all points A, B and C are sagging down obviously at $Fr = 0.5$, while only slight sagging is observed for point A at $Fr = 0.2$ due to the effect of the upward tension force. As a result, the amplitude of Y' is increasing from point A to point C at $Fr = 0.2$, while no difference at $Fr = 0.5$.

However, at $Fr = 1.0$, the flag is wholly sagging down as shown in figure 19(*c*). The sagging flag has only a small-amplitude rigid flapping in the y direction due to the fluid loading, except that the upper corner is rolling up irregularly by disturbance of the surrounding fluid, as can be seen in figure 18(*c*). The suppression of the flapping motion indicates that gravity of the flag overwhelms the pressure difference across the flag in this case. The stabilization effect of gravity can be understood by resorting to a hanging flag in an axial flow, where gravity is directed along the streamwise direction. Following the linear stability analysis of a two-dimensional flag in a uniform axial flow by Connell & Yue (2007), the criterion for existence of flapping can be written

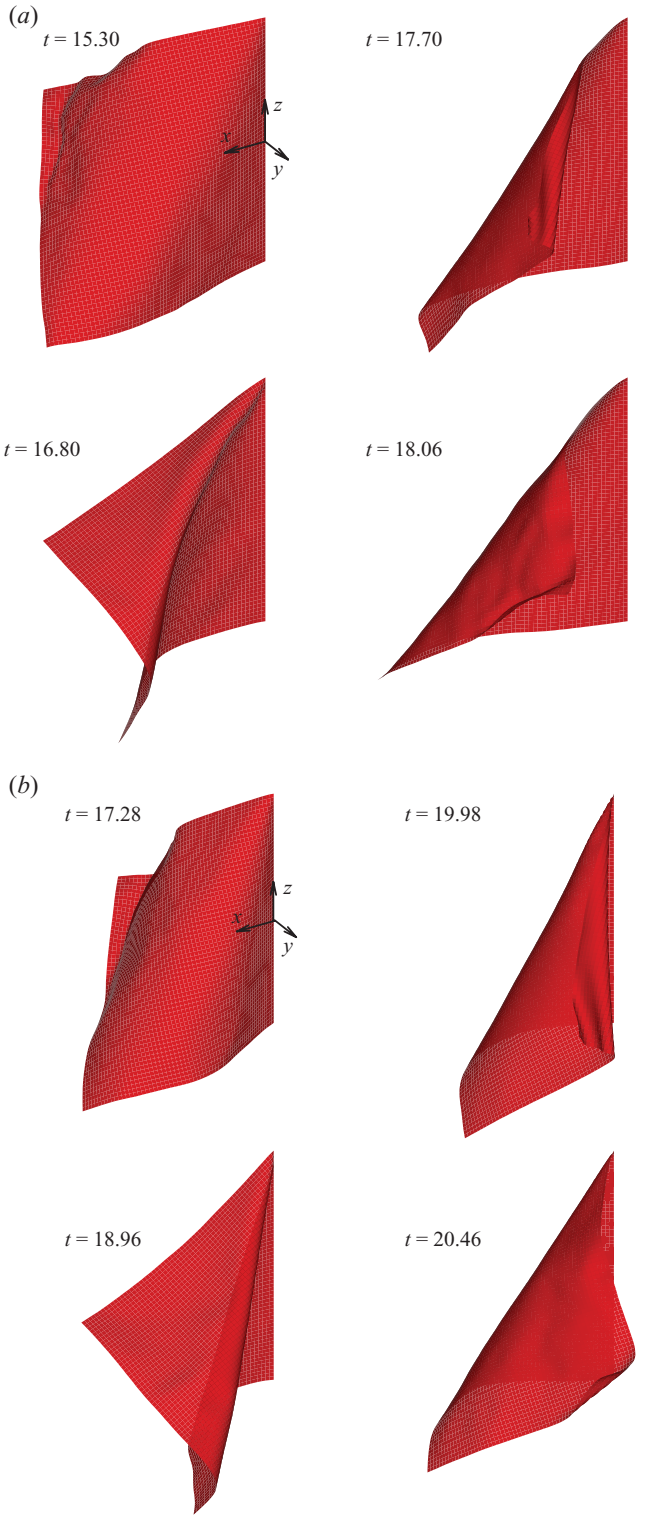

FIGURE 19. (Colour online) For caption see next page.

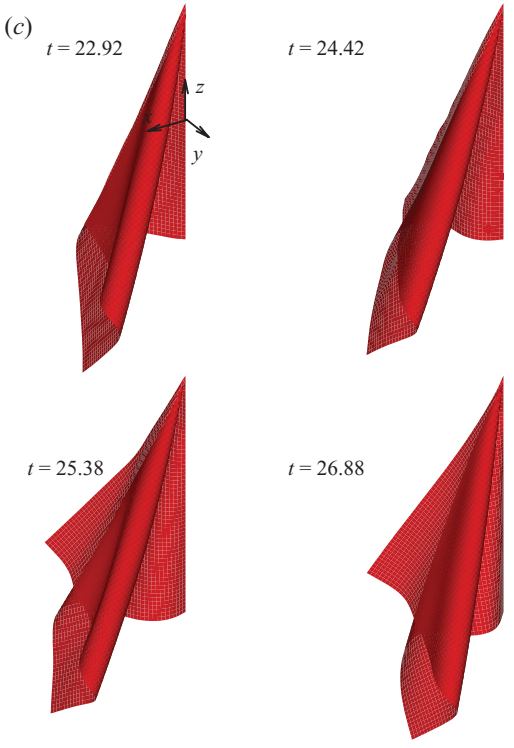

FIGURE 19. (Colour online) Instantaneous positions of a flapping flag at the four instants as labelled in figure 18 for $Re = 200$: (*a*) $Fr = 0.2$; (*b*) $Fr = 0.5$; (*c*) $Fr = 1.0$. Supplementary movie 6 available at journals.cambridge.org/flm.

as

$$\frac{\rho}{\rho + c_m} > \tilde{\sigma} + \tilde{\gamma} k^2, \tag{25}$$

where $c_m = m_a/\rho_0 L$ with m_a the added mass, $\tilde{\sigma}$ denotes the tension force, $\tilde{\gamma}$ denotes the bending rigidity, k denotes the wavenumber and all quantities are dimensionless. Note that the flag motion equation (3) is non-dimensionalized using the flag density ρ_1 as the characteristic density, while the fluid density ρ_0 is adopted in non-dimensionalization of (25), i.e. $\rho_0 U_\infty^2 L$ for the tension force and $\rho_0 U_\infty^2 L^3$ for the bending rigidity. The tension force induced by the viscous shear is written as $1.3\rho_0 U_\infty^2 L Re^{-0.5}(1-\sqrt{x/L})$, and $\rho_1 g(L-x)$ by gravity. Taking the maximum value and making non-dimensionalization, we have

$$\tilde{\sigma} = 1.3 Re^{-0.5} + \rho Fr. \tag{26}$$

By substituting (26) into (25), we can easily see that the fluid–flag system is more stable after including gravity. Despite of the obvious difference between the present computational model and the hanging flag in an axial flow, some similarities can be found because the sagging flag has an inclined angle with the free stream, which can be decomposed into the components parallel and normal to the flag, and so does gravity. Firstly, the longitudinal tension force is increased by gravity which competes with the pressure difference and stabilizes the flag. As Fr increases, the flag is more sagging down, so the parallel component of gravity increases while that of the free stream decreases. Secondly, the effect of ρ changes after including gravity. In the gravity-free cases, the fluid–flag system becomes more unstable as ρ increases, as

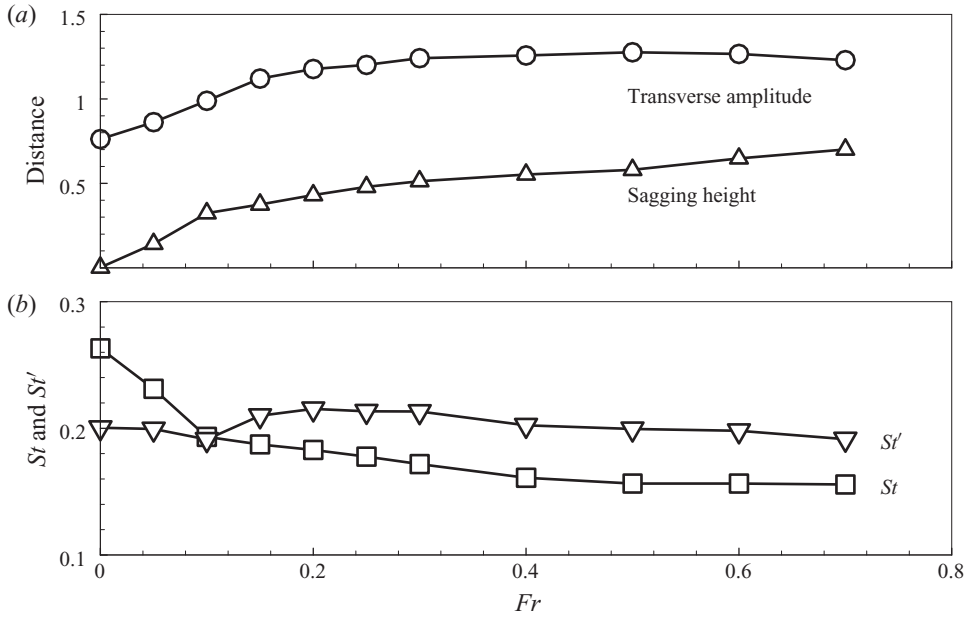

FIGURE 20. Variations of (*a*) the flapping amplitude and sagging distance and (*b*) Strouhal number with Fr at $Re = 200$.

dictated in (25). However, after including gravity, the system becomes more stable as ρ increases if Fr is larger than a certain value, which can be seen easily by substituting (26) into (25) and was also observed in our simulations (results not shown here).

For regular flapping under gravity, effects of the Froude number on the transverse flapping amplitude of point C (denoted by A_C), the average sagging height of point C (denoted by S_h) and the Strouhal number (St and St' defined in (23)) are represented in figure 20. As Fr increases, both A_C and S_h are increased as shown in figure 20(*a*), while St is decreased as shown in figure 20(*b*). As a result, the Strouhal number (St') based on the flapping amplitude remains close to 0.2 as Fr increases, similar to the effect of increasing the flag density for the gravity-free cases. Since the flag is straight and stationary stable if given a small density, we expect that the flag is destabilized after including gravity. The destabilization effect of gravity is obvious at first glance, because the flag cannot almost resist the spanwise loading in the straight state. Note also the difference between the present configuration and the hanging flag in axial flow as mentioned above. In the hanging-flag case, gravity is mainly balanced by the longitudinal tension like a pendulum. As Fr increases, the flapping amplitude is decreased while the flapping frequency is increased by taking into account both the fluid loading and gravity. However, in the present configuration which is more prevalent in real situation, the relationship among the various force terms as dictated in the flag motion equation (4) becomes more complicate during regular flapping. As an example to demonstrate the destabilization effect of gravity, we choose a light flag of $\rho = 0.2$. Figure 21 shows time histories of Y of points A, B and C for $Re = 200$. At $Fr = 0$ (figure 21*a*), it is shown that the flapping motion is decaying fast. Interestingly, a stable flapping motion is established with a phase difference among points A, B and C at $Fr = 0.5$ after an initial transition stage (figure 21*b*). The instantaneous flag positions plotted in figure 22 show that a travelling wave in the upper-forward direction is formed on the flag under gravity. In this case, the pressure difference across

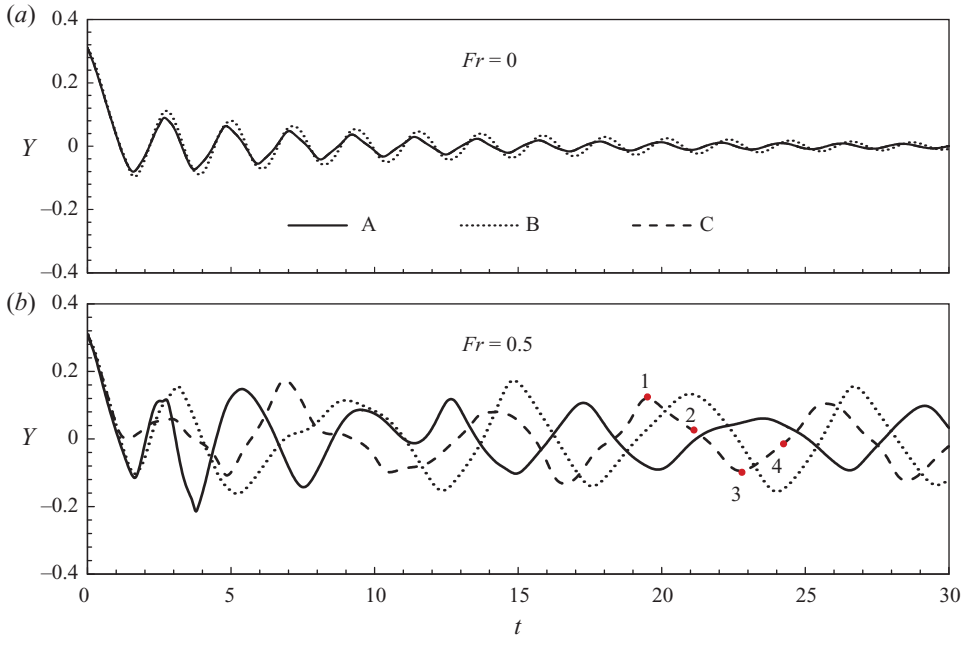

FIGURE 21. Time histories of the transverse position of points A, B and C (figure 1) for $\rho = 0.2$ and $Re = 200$: (*a*) $Fr = 0$; (*b*) $Fr = 0.5$. Points 1, 2, 3 and 4 correspond sequentially to the four instants adopted in figure 22.

the flag is balanced by gravity of the flag, besides its inertia which is small. Figure 23 compares the pressure contours of $Fr = 0$ and 0.5 in the xy plane of $z = 0$, where the flag position is obtained by interpolation. It is shown that there is no positive pressure on both sides of the flag behind the stagnation point, since the inclined angle of the flag to the free stream is small for both cases. However, the pressure magnitude is obviously increased after including gravity, and so does the pressure difference across the flag, which together with gravity induces large deformation of the flag.

4. Conclusions

In this paper, we proposed a three-dimensional computational model for simulating the flag motion in a uniform flow. The flag motion equation was derived by the energy method and was solved on a Lagrangian grid. On the other hand, the fluid motion was governed by the Navier–Stokes equations described on an Eulerian coordinate. The full coupled system was simulated using the immersed boundary method. Using our computational data, the nonlinear dynamics of the fluid–flag system after setting up of flapping was investigated. In the simulations, the flag is vertically supported at its leading edge. When gravity is excluded, the flag flaps symmetrically about its centreline at low Reynolds numbers. A longitudinal travelling wave is formed on the flag, which flattens the deformation in the spanwise direction. Thus, the spanwise bending was only observed close to the corners on the trailing edge. Due to the decrease of the viscous force of the fluid and the increase of the pressure difference across the flag, the trailing edge is more flattened as the Reynolds number increases. At a certain critical Reynolds number, the flag loses its symmetry about its centreline, which is attributed to the coupled fluid–flag instability. Moreover, a backward travelling wave

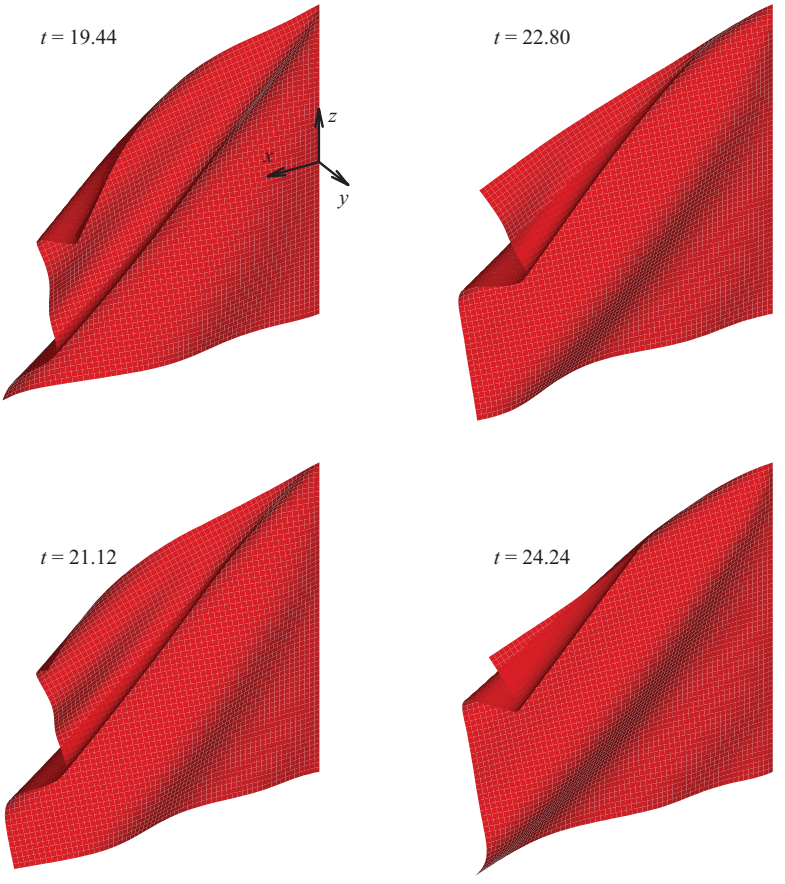

FIGURE 22. (Colour online) Instantaneous positions of a flapping flag at the four instants as labelled in figure 21 for $\rho = 0.2$, $Re = 200$ and $Fr = 0.5$. Supplementary movie 7 available at journals.cambridge.org/flm.

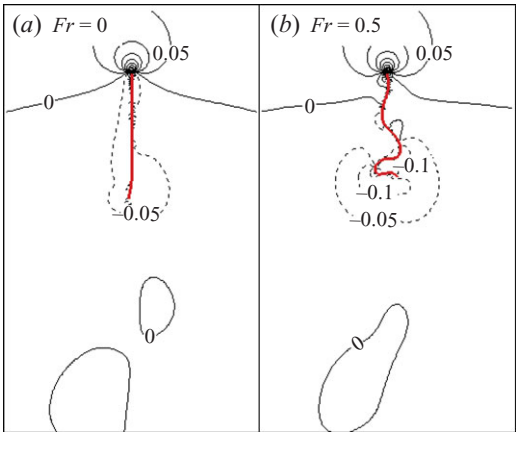

FIGURE 23. (Colour online) Pressure contours near the flag in the xy plane of $z = 0$ at instant 1 as labelled in figure 22 for $\rho = 0.2$ and $Re = 200$: (*a*) $Fr = 0$; (*b*) $Fr = 0.5$.

was observed when the flag inertia dominates over the viscous force of the surrounding fluid. The three-dimensional vortical structures shed from the flag show a significant difference from the results of two-dimensional simulations. By the flapping of the two side edges, the longitudinal components are generated. Consequently, hairpin or O-shaped structures are shed from the flag as a whole, which play an important role in the dynamics of the fluid–flag system. The three-dimensional vortical structures cause the decrease of the pressure difference across the flag and the bending of the trailing edge, thus stabilizing the flag as compared with the two-dimensional case. The loss of symmetry of the flag about its centreline was also explained by looking at the acceleration of the fluid at the trailing edge. Then, the flapping frequency was studied using two Strouhal numbers, defined in terms of the flag length or the flapping amplitude (denoted by St and St', respectively). It was shown that St is invariant to Re, indicating that the flag inertia dominates over the viscous force exerted on the flag by the surrounding fluid. For this reason, St is changed only slightly for different flag width but is decreased as ρ increases, consistent with the scaling law $St \sim \rho^{-1/2}$. On the other hand, St' remains constant close to 0.2, which is consistent with the values reported for flying or swimming animals. It was supposed that the universal Strouhal number is a result of wake instability for the onset of vortex shedding. Moreover, as H increases, convergences of St, A and St' to the two-dimensional results are improved for large ρ. After including gravity directing along the negative spanwise direction, the sagging down of the flag and the rolling motion of the upper corner were observed. Unlike the gravity-free cases, apparent phase difference was seen for the top, middle and bottom points on the trailing edge due to the sagging of flag. For regular flapping under gravity, the flapping amplitude and the sagging height are increased but St is decreased as Fr increases, while St' is still close to 0.2. Given a too large Fr, however, the flag is wholly sagging down without a sustained regular flapping. Hence, it was demonstrated that gravity has dual effects on the flag stability. On one side it has a destabilization effect like the flag inertia, which was explained by resorting to the linear stability analysis of a hanging flag in an axial flow. On the other side, gravity has a stabilization effect by increasing the longitudinal tension force. It was shown that a flag is straight and stationary stable without gravity if given a small density, but a regular inclined travelling wave is established on the flag by including gravity, which induces an increased pressure difference across the flag.

This work was supported by the Creative Research Initiatives (Centre for Opto-Fluid-Flexible Body Interaction) of MEST/NRF.

Appendix A

Perturbation of the energy functional $E(\boldsymbol{X})$ in (1) can be expressed as

$$\wp E(\boldsymbol{X}) = \wp \int_S \sum_{i,j=1}^{2} \left[c_{ij}^T \left(T_{ij} - T_{ij}^0 \right)^2 + c_{ij}^B \left(B_{ij} - B_{ij}^0 \right)^2 \right] \mathrm{d}s_1 \, \mathrm{d}s_2. \tag{A 1}$$

By applying the perturbation operation $\wp$ to the first term on the right-hand side of (A 1), we obtain

$$\wp \int_S c_{ij}^T \left(T_{ij} - T_{ij}^0 \right)^2 \mathrm{d}s_1 \, \mathrm{d}s_2 = \int_S 2 c_{ij}^T \left(T_{ij} - T_{ij}^0 \right) \wp T_{ij} \, \mathrm{d}s_1 \, \mathrm{d}s_2 = \int_S \sigma_{ij} \frac{\partial \boldsymbol{X}}{\partial s_i} \cdot \frac{\partial \wp \boldsymbol{X}}{\partial s_j} \, \mathrm{d}s_1 \, \mathrm{d}s_2, \tag{A 2}$$

where we defined $\sigma_{ij} = 4c_{ij}^T(T_{ij} - T_{ij}^0)$ and used $T_{ij} = (\partial \boldsymbol{X}/\partial s_i \cdot \partial \boldsymbol{X}/\partial s_j)$. Here the summation convention is not applied on i and j $(i, j = 1, 2)$. Using integration by parts, (A 2) becomes

$$\wp \int_S c_{ij}^T \left(T_{ij} - T_{ij}^0\right)^2 \mathrm{d}s_1\, \mathrm{d}s_2 = \int_S \frac{\partial}{\partial s_i}\left(\sigma_{ij}\frac{\partial \boldsymbol{X}}{\partial s_j} \cdot \wp \boldsymbol{X}\right)\mathrm{d}s_1\, \mathrm{d}s_2 - \int_S \frac{\partial}{\partial s_i}\left(\sigma_{ij}\frac{\partial \boldsymbol{X}}{\partial s_j}\right) \cdot \wp \boldsymbol{X}\mathrm{d}s_1\, \mathrm{d}s_2, \tag{A 3}$$

where the first term on the right-hand side can be eliminated by using

$$\begin{cases} \wp \boldsymbol{X} = 0 & \text{at the fixed boundary,} \\ \sigma_{ij} = 0 & \text{at the free boundaries.} \end{cases} \tag{A 4}$$

Then we apply the perturbation operation $\wp$ to the second term on the right-hand side of (A 1) and integrate by parts once, yielding

$$\wp \int_S c_{ij}^B \left(B_{ij} - B_{ij}^0\right)^2 \mathrm{d}s_1\, \mathrm{d}s_2 = \int_S \gamma_{ij}\frac{\partial^2 \boldsymbol{X}}{\partial s_i \partial s_j} \cdot \frac{\partial^2 \wp \boldsymbol{X}}{\partial s_i \partial s_j}\, \mathrm{d}s_1\, \mathrm{d}s_2$$

$$= \int_S \frac{\partial}{\partial s_j}\left(\gamma_{ij}\frac{\partial^2 \boldsymbol{X}}{\partial s_i \partial s_j} \cdot \frac{\partial \wp \boldsymbol{X}}{\partial s_i}\right)\mathrm{d}s_1\, \mathrm{d}s_2 - \int_S \frac{\partial}{\partial s_j}\left(\gamma_{ij}\frac{\partial^2 \boldsymbol{X}}{\partial s_i \partial s_j}\right) \cdot \frac{\partial \wp \boldsymbol{X}}{\partial s_i}\, \mathrm{d}s_1\, \mathrm{d}s_2, \tag{A 5}$$

where we defined $\gamma_{ij} = 2c_{ij}^B$. If the fixed boundary is simply supported, we have

$$\begin{cases} \wp \boldsymbol{X} = 0,\ \dfrac{\partial^2 \boldsymbol{X}}{\partial s_1^2} = 0,\ \dfrac{\partial}{\partial s_2} = 0 & \text{at the fixed boundary,} \\ \dfrac{\partial^2 \boldsymbol{X}}{\partial s_i^2} = 0,\ \dfrac{\partial^3 \boldsymbol{X}}{\partial s_i^3} = 0,\ \gamma_{ij} = 0 & \text{at the free boundaries.} \end{cases} \tag{A 6}$$

Otherwise, if the fixed boundary is clamped, we have

$$\begin{cases} \wp \boldsymbol{X} = \dfrac{\partial \wp \boldsymbol{X}}{\partial s_i} = 0 & \text{at the fixed boundary,} \\ \dfrac{\partial^2 \boldsymbol{X}}{\partial s_i^2} = 0,\ \dfrac{\partial^3 \boldsymbol{X}}{\partial s_i^3} = 0,\ \gamma_{ij} = 0 & \text{at the free boundaries.} \end{cases} \tag{A 7}$$

Using either (A 6) or (A 7), the first term on the right-hand side of (A 5) is eliminated. Applying integration by parts once again to (A 5) results in

$$\wp \int_S c_{ij}^B \left(B_{ij} - B_{ij}^0\right)^2 \mathrm{d}s_1\, \mathrm{d}s_2 = -\int_S \frac{\partial^2}{\partial s_i \partial s_j}\left(\gamma_{ij}\frac{\partial^2 \boldsymbol{X}}{\partial s_i \partial s_j} \cdot \wp \boldsymbol{X}\right)\mathrm{d}s_1\, \mathrm{d}s_2$$

$$+ \int_S \frac{\partial^2}{\partial s_i \partial s_j}\left(\gamma_{ij}\frac{\partial^2 \boldsymbol{X}}{\partial s_i \partial s_j}\right) \cdot \wp \boldsymbol{X}\, \mathrm{d}s_1\, \mathrm{d}s_2, \tag{A 8}$$

where the first term on the right-hand side is also eliminated by using either (A 6) or (A 7). In summary, perturbation of the energy functional $E(X)$ results in

$$\wp E(\boldsymbol{X}) = -\int_S \left[\frac{\partial}{\partial s_i}\left(\sigma_{ij}\frac{\partial \boldsymbol{X}}{\partial s_j}\right) - \frac{\partial^2}{\partial s_i \partial s_j}\left(\gamma_{ij}\frac{\partial^2 \boldsymbol{X}}{\partial s_i \partial s_j}\right)\right] \cdot \wp \boldsymbol{X}\, \mathrm{d}s_1\, \mathrm{d}s_2. \tag{A 9}$$

According to the principle of virtual work, the elastic force is expressed as

$$\boldsymbol{F_e} = -\frac{\wp E(\boldsymbol{X})}{\wp \boldsymbol{X}}. \tag{A 10}$$

Thus the differential form of the elastic force is obtained as given in (2). As shown above, (2) is valid for both free and fixed boundary conditions, and the fixed condition can be further classified into simply-supported and clamped conditions.

Appendix B

The Lagrangian coordinate system is shown in figure 1, where the indices of the Lagrangian points are denoted by (I, J) in the (s_1, s_2) directions, respectively. Note that the structure domain is discretized by a non-uniform grid in Huang & Sung (2009), but here we just use a uniform grid since the flag is assumed to be inextensible. Let D_1 and D_2 denote the difference approximations to the first-order derivatives of the arc lengths s_1 and s_2, respectively. Specifically, for an arbitrary variable ϕ, the downwind and upwind difference approximations of the arclength s_1 are denoted by, respectively,

$$[D_1^+\phi]_{I,J} = (\phi_{I+1,J} - \phi_{I,J})/\Delta s_1, \tag{B 1}$$

$$[D_1^-\phi]_{I,J} = (\phi_{I,J} - \phi_{I-1,J})/\Delta s_1. \tag{B 2}$$

In the same way, we can define D_2^+ and D_2^-. Thus, the second-order central difference approximations are expressed as

$$\left[D_{11}^0\phi\right]_{I,J} = \left[D_1^+D_1^-\phi\right]_{I,J} = (\phi_{I+1,J} - 2\phi_{I,J} + \phi_{I-1,J})/\Delta s_1^2 \tag{B 3}$$

and

$$\left[D_{22}^0\phi\right]_{I,J} = \left[D_2^+D_2^-\phi\right]_{I,J} = (\phi_{I,J+1} - 2\phi_{I,J} + \phi_{I,J-1})/\Delta s_2^2. \tag{B 4}$$

The second-order cross difference approximations are

$$[D_{12}^+\phi]_{I,J} = [D_1^+D_2^+\phi]_{I,J} = (\phi_{I+1,J+1} - \phi_{I+1,J} - \phi_{I,J+1} + \phi_{I,J})/\Delta s_1\,\Delta s_2, \tag{B 5}$$

$$[D_{12}^-\phi]_{I,J} = [D_1^-D_2^-\phi]_{I,J} = (\phi_{I,J} - \phi_{I-1,J} - \phi_{I,J-1} + \phi_{I-1,J-1})/\Delta s_1\,\Delta s_2, \tag{B 6}$$

and we have $[D_{21}^+\phi]_{I,J} = [D_{12}^+\phi]_{I,J}$ and $[D_{21}^-\phi]_{I,J} = [D_{12}^-\phi]_{I,J}$.

The stretching force terms in (4) are discretized as

$$\frac{\partial}{\partial s_i}\left(\sigma_{ii}\frac{\partial \boldsymbol{X}}{\partial s_i}\right) = D_i^-\left(\boldsymbol{\sigma}_{ii}D_i^+\boldsymbol{X}\right) + O\left(\Delta s_i^2\right), \quad (i = 1, 2), \tag{B 7}$$

where $\sigma_{ii} = \varphi_{ii}(T_{ii} - 1)$ and $T_{ii} = D_i^+\boldsymbol{X}\cdot D_i^+\boldsymbol{X}$. Moreover, the shearing force terms are discretized as, respectively,

$$\frac{\partial}{\partial s_1}\left(\sigma_{12}\frac{\partial \boldsymbol{X}}{\partial s_2}\right) = \frac{1}{2}\left[D_1^-\left(\sigma_{12}^+D_2^+\boldsymbol{X}\right) + D_1^-\left(\sigma_{12}^-D_2^-\boldsymbol{X}\right)\right] + O\left(\Delta s_1, \Delta s_2^2/\Delta s_1\right), \tag{B 8}$$

$$\frac{\partial}{\partial s_2}\left(\sigma_{21}\frac{\partial \boldsymbol{X}}{\partial s_1}\right) = \frac{1}{2}\left[D_2^-\left(\sigma_{21}^+D_1^+\boldsymbol{X}\right) + D_2^+\left(\sigma_{21}^-D_1^+\boldsymbol{X}\right)\right] + O\left(\Delta s_1, \Delta s_2^2/\Delta s_1\right), \tag{B 9}$$

where $\sigma_{12}^+ = \sigma_{21}^+ = \varphi_{12}D_1^+\boldsymbol{X}\cdot D_2^+\boldsymbol{X}$ and $\sigma_{12}^- = \sigma_{21}^- = \varphi_{12}D_1^+\boldsymbol{X}\cdot D_2^-\boldsymbol{X}$. Furthermore, discretizations of the bending force terms are written as

$$\frac{\partial^2}{\partial s_i^2}\left(\gamma_{ii}\frac{\partial^2 \boldsymbol{X}}{\partial s_i^2}\right) = D_{ii}^0\left(\gamma_{ii}D_{ii}^0\boldsymbol{X}\right) + O\left(\Delta s_i^2\right), \quad (i = 1, 2), \tag{B 10}$$

and the twisting force terms are equivalent to each other, which are discretized as

$$\frac{\partial^2}{\partial s_1\partial s_2}\left(\gamma_{12}\frac{\partial^2 \boldsymbol{X}}{\partial s_1\partial s_2}\right) = \frac{\partial^2}{\partial s_2\partial s_1}\left(\gamma_{21}\frac{\partial^2 \boldsymbol{X}}{\partial s_2\partial s_1}\right) = D_{12}^-\left(\gamma_{12}D_{12}^+\boldsymbol{X}\right) + O\left(\Delta s_1^2, \Delta s_2^2\right). \tag{B 11}$$

Thus, the elastic force $\boldsymbol{F}_e$ is obtained by summing (B 7)–(B 11). We use the operator K to represent the discretized form of $\boldsymbol{F}_e$, i.e.

$$\boldsymbol{F}_e = K\boldsymbol{X}. \tag{B 12}$$

Note that the stencil used here for discretization of $\boldsymbol{F}_e$ is symmetric in the s_2 direction in order to avoid numerical errors that cause asymmetry of the flag about its centreline in the simulation.

Supplementary movies are available at journals.cambridge.org/flm

REFERENCES

Alben, S. & Shelley, M. J. 2008 Flapping states of a flag in an inviscid fluid: bistability and the transition to chaos. *Phys. Rev. Lett.* **100**, 074301.

Allen, J. J. & Smits, A. J. 2001 Energy harvesting eel. *J. Fluids Struct.* **15**, 629–640.

Argentina, M. & Mahadevana, L. 2005 Fluid-flow-induced flutter of a flag. *PNAS* **102**, 1829–1834.

Balint, T. S. & Lucey, A. D. 2005 Instability of a cantilevered flexible plate in viscous channel flow. *J. Fluids Struct.* **20**, 893–912.

Beal, D. N., Hover, F. S., Triantafyllou, M. S., Liao, J. C. & Lauder G. V. 2006 Passive propulsion in vortex wakes. *J. Fluid Mech.* **549**, 385–402.

Connell, B. S. H. & Yue, D. K. P. 2007 Flapping dynamics of a flag in a uniform stream. *J. Fluid Mech.* **581**, 33–67.

Eldredge, J. D. & Pisani, D. 2008 Passive locomotion of a simple articulated fish-like system in the wake of an obstacle. *J. Fluid Mech.* **607**, 279–288.

Eloy, C., Lagrange, R., Souilliez, C. & Schouveiler, L. 2008 Aeroelastic instability of cantilevered flexible plates in uniform flow. *J. Fluid Mech.* **611**, 97–106.

Eloy, C., Souilliez, C. & Schouveiler, L. 2007 Flutter of a rectangular plate. *J. Fluids Struct.* **23**, 904–919.

Farnell, D. J. J., David, T. & Barton, D. C. 2004 Numerical simulations of a filament in a flowing soap film. *Intl J. Numer. Methods Fluids* **44**, 313–330.

Fish, F. E. & Lauder, G. V. 2006 Passive and active flow control by swimming fishes and mammals. *Annu. Rev. Fluid Mech.* **38**, 193–224.

Goldstein, D., Handler, R. & Sirovich, L. 1993 Modeling a no-slip flow boundary with an external force field. *J. Comput. Phys.* **105**, 354–366.

Guo, C. Q. & Païdoussis, M. P. 2000 Stability of rectangular plates with free side-edges in two-dimensional inviscid channel flow. *Trans. ASME: J. Appl. Mech.* **67**, 171–176.

Huang, L. 1995 Flutter of cantilevered in axial flow. *J. Fluids Struct.* **9**, 127–147.

Huang, W.-X., Shin, S. J. & Sung, H. J. 2007 Simulation of flexible filaments in a uniform flow by the immersed boundary method. *J. Comput. Phys.* **226**, 2206–2228.

Huang, W.-X. & Sung, H. J. 2009 An immersed boundary method for fluid-flexible structure interaction. *Comput. Methods Appl. Mech. Engng* **198**, 2650–2661.

Jeong, J. & Hussain, F. 1995 On the identification of a vortex. *J. Fluid Mech.* **285**, 69–94.

Jia, L.-B., Li, F., Yin, X.-Z. & Yin, X.-Y. 2007 Coupling modes between two flapping filaments. *J. Fluid Mech.* **581**, 199–220.

Jia, L.-B. & Yin, X.-Z. 2008 Passive oscillations of two tandem flexible filaments in a flowing soap film. *Phys. Rev. Lett.* **100**, 228104.

Kim, K., Baek, S.-J. & Sung, H. J. 2002 An implicit velocity decoupling procedure for incompressible Navier–Stokes equations. *Intl J. Numer. Methods Fluids* **38**, 125–138.

Kim, Y. & Peskin, C. S. 2007 Penalty immersed boundary method for an elastic boundary with mass. *Phys. Fluids* **19**, 053103.

Lemaitre, C., Hémon, P. & de Langre, E. 2005 Instability of a long ribbon hanging in axial air flow. *J. Fluids Struct.* **20**, 913–925.

Li, L., Damodaran, M. & Gay, R. K. L. 1996 Aerodynamic force models for animating cloth motion in air flow. *The Vis. Comput.* **12**, 84–104.

Liao, J. C., Beal, D. N., Lauder, G. V. & Triantafyllou, M. S. 2003 Fish exploiting vortices decrease muscle activity. *Science* **302**, 1566–1569.

Manela, A. & Howe, M. S. 2009*a* On the stability and sound of an unforced flag, *J. Sound Vib.* **321**, 994–1006.

Manela, A. & Howe, M. S. 2009*b* The forced motion of a flag, *J. Fluid Mech.* **635**, 439–454.

Michelin, S., Llewellyn Smith, S. G. & Glover, B. J. 2008 Vortex shedding model of a flapping flag. *J. Fluid Mech.* **617**, 1–10.

Païdoussis, M. P. 2004 *Fluid–Structure Interaction: Slender Structures and Axial Flow*, vol. 2, Academic.

Peskin, C. S. 2002 The immersed boundary method. *Acta Numer.* 479–517.

Ristroph, L. & Zhang, J. 2008 Anomalous hydrodynamic drafting of interacting flapping flags. *Phys. Rev. Lett.* **101**, 194502.

Shelley, M., Vandenberghe, N. & Zhang, J. 2005 Heavy flags undergo spontaneous oscillations in flowing water. *Phys. Rev. Lett.* **94**, 094302.

Taneda, S. 1968 Waving motion of flags. *J. Phys. Soc. Japan* **24** (2), 392–401.

Tang, L. & Païdoussis, M. P. 2007 On the instability and the post-critical behaviour of two-dimensional cantilevered flexible plates in axial flow. *J. Sound Vib.* **305**, 97–115.

Tang, D. M., Yamamoto, H. & Dowell, E. H. 2003 Flutter and limit cycle oscillations of two-dimensional panels in three-dimensional axial flow. *J. Fluids Struct.* **17**, 225–242.

Taylor, G. W., Burns, J. R., Kammann, S. M., Powers, W. B. & Welsh, T. R. 2001 The energy harvesting eel: a small subsurface ocean/river power generator. *IEEE J. Ocean. Engng* **26** (4), 539–547.

Taylor, G. K., Nudds, R. L. & Thomas, A. L. R. 2003 Flying and swimming animals cruise at a Strouhal number tuned for high power efficiency. *Nature* **425,** 707–711.

Terzopoulos, D. & Fleischer, K. 1988 Deformable models. *The Vis. Comput.* **4**, 306–331.

Triantafyllou, M. S., Triantafyllou, G. S. & Yue, D. K. P. 2000 Hydrodynamics of fishlike swimming. *Annu. Rev. Fluid Mech.* **32**, 33–53.

Watanabe, Y., Isogai, K., Suzuki, S. & Sugihara, M. 2002*a* A theoretical study of paper flutter. *J. Fluids Struct.* **16**, 543–560.

Watanabe, Y., Suzuki, S., Sugihara, M. & Sueoka, Y. 2002*b* An experimental study of paper flutter. *J. Fluids Struct.* **16**, 529–542.

Williamson, C. H. K. 1996 Vortex dynamics in the cylinder wake. *Annu. Rev. Fluid Mech.* **28**, 477–539.

Yadykin, Y., Tenetov, V. & Levin, D. 2001 The flow-induced vibration of a flexible strip hanging vertically in a parallel flow. Part 1. Temporal aeroelastic instability. *J. Fluids Struct.* **15**, 1167–1185.

Zhang, J., Childress, S., Libchaber, A. & Shelley, M. 2000 Flexible filaments in a flowing soap film as a model for one-dimensional flags in a two-dimensional wind. *Nature* **408**, 835–839.

Zhu, L. & Peskin, C. S. 2002 Simulation of a flapping flexible filament in a flowing soap film by the immersed boundary method. *J. Comput. Phys.* **179**, 452–468.